Effect of Storm Size on Sea Surface Cooling and Tropical Cyclone Intensification in the Western North Pacific

YUHAO LIU,[a] SHOUDE GUAN,[a,b] I.-I. LIN,[c] WEI MEI,[d] FEI-FEI JIN,[e] MENGYA HUANG,[a] YIHAN ZHANG,[a] WEI ZHAO,[a,b] AND JIWEI TIAN[a,b]

[a] *Frontier Science Center for Deep Ocean Multispheres and Earth System (FDOMES) and Physical Oceanography Laboratory/ Key Laboratory of Ocean Observation and Information of Hainan Province, Sanya Oceanographic Institution, Ocean University of China, Qingdao/Sanya, China*
[b] *Laoshan Laboratory, Qingdao, China*
[c] *Department of Atmospheric Sciences, National Taiwan University, Taipei, Taiwan*
[d] *Department of Earth, Marine and Environmental Sciences, University of North Carolina at Chapel Hill, Chapel Hill, North Carolina*
[e] *Department of Atmospheric Sciences, SOEST, University of Hawai'i at Mānoa, Honolulu, Hawaii*

(Manuscript received 26 December 2022, in final form 13 July 2023, accepted 17 July 2023)

ABSTRACT: The effect of tropical cyclone (TC) size on TC-induced sea surface temperature (SST) cooling and subsequent TC intensification is an intriguing issue without much exploration. Via compositing satellite-observed SST over the western North Pacific during 2004–19, this study systematically examined the effect of storm size on the magnitude, spatial extension, and temporal evolution of TC-induced SST anomalies (SSTA). Consequential influence on TC intensification is also explored. Among the various TC wind radii, SSTA are found to be most sensitive to the 34-kt wind radius (R34) (1 kt $\approx$ 0.51 m s^{-1}). Generally, large TCs generate stronger and more widespread SSTA than small TCs (for category 1–2 TCs, R34: ~270 vs 160 km; SSTA: −1.7° vs −0.9°C). Despite the same effect on prolonging residence time of TC winds, the effect of doubling R34 on SSTA is more profound than halving translation speed, due to more wind energy input into the upper ocean. Also differing from translation speed, storm size has a rather modest effect on the rightward shift and timing of maximum cooling. This study further demonstrates that storm size regulates TC intensification through an oceanic pathway: large TCs tend to induce stronger SST cooling and are exposed to the cooling for a longer time, both of which reduce the ocean's enthalpy supply and thereby diminish TC intensification. For larger TCs experiencing stronger SST cooling, the probability of rapid intensification is half of smaller TCs. The presented results suggest that accurately specifying storm size should lead to improved cooling effect estimation and TC intensity prediction.

SIGNIFICANCE STATEMENT: Storm size has long been speculated to play a crucial role in modulating the TC self-induced sea surface temperature (SST) cooling and thus potentially influence TC intensification through ocean negative feedback. Nevertheless, systematic analysis is lacking. Here we show that larger TCs tend to generate stronger SST cooling and have longer exposure to the cooling effect, both of which enhance the strength of the negative feedback. Consequently, larger TCs undergo weaker intensification and are less likely to experience rapid intensification than smaller TCs. These results demonstrate that storm size can influence TC intensification not only from the atmospheric pathway, but also via the oceanic pathway. Accurate characterization of this oceanic pathway in coupled models is important to accurately forecast TC intensity.

KEYWORDS: North Pacific Ocean; Atmosphere-ocean interaction; Hurricanes/typhoons; Sea surface temperature; Tropical cyclones

1. Introduction

Tropical cyclones (TCs) are destructive natural disasters (Emanuel 2003). The strong winds associated with TCs can effectively stir the stratified upper ocean and produce significant sea surface temperature (SST) cooling and subsurface water warming (Price 1981). The earliest report on measuring SST cooling after TC passage can be dated back to the 1960s, wherein Leipper (1967) conducted a systematic survey on Hurricane Hilda (1964) and showed an approximately 5°C SST reduction. Since then, many observational analyses and numerical simulations have been devoted to exploring the TC-induced SST cooling, owing to its important effects in many aspects, such as on storm intensification (e.g., Lloyd and Vecchi 2011; Dare and McBride 2011; Lin et al. 2008, 2013; Mei et al. 2012, 2015a) and ocean heat uptake (e.g., Emanuel 2001; Sriver and Huber 2007; Korty et al. 2008; Mei et al. 2013; Zhang et al. 2019).

The warm ocean is the energy source for TC development, and TCs draw energy and moisture from the ocean through the enthalpy flux at the air–sea interface (Emanuel 1999). Meanwhile, most of the kinetic energy of TCs is lost via friction at the air–sea interface, driving strong sheared currents and triggering vigorous vertical mixing in the upper ocean (Emanuel 2003). The triggered vertical mixing acts to bring

Supplemental information related to this paper is available at the Journals Online website: https://doi.org/10.1175/JCLI-D-22-0949.s1.

Corresponding author: Shoude Guan, guanshoude@ouc.edu.cn

DOI: 10.1175/JCLI-D-22-0949.1

cold subsurface water to the sea surface and significantly reduce the SST beneath the storms (e.g., Price 2009; Pun et al. 2011; D'Asaro et al. 2011, 2014; Zhang et al. 2016). Both observational analyses and numerical experiments demonstrate that the TC-induced SST cooling could significantly reduce the enthalpy flux from the ocean to the air and thus suppress the subsequent intensification of the TC, which is known as the negative SST feedback (e.g., Schade 2000; Cione and Uhlhorn 2003; Jacob and Shay 2003; Lloyd and Vecchi 2011; Mei et al. 2012; Lin et al. 2013). The strength of the negative SST feedback critically depends on the magnitude of the SST cooling. Based on in situ observations, Cione and Uhlhorn (2003) indicates that a modest 1°C cooling can reduce the surface enthalpy flux by 40%, while a 2.5°C cooling would be sufficient to entirely shut down the energy supply to the TC (Emanuel 1999). Therefore, an accurate representation of the TC-induced SST cooling during the TC passage is of vital importance for improving TC intensity prediction, as has been confirmed by operational forecasting models (Bender and Ginis 2000; Shen and Ginis 2003; Emanuel et al. 2004; Goni et al. 2009).

After the TC passage, the produced sea surface cooling usually persists for several days to one month before recovering to climatological SST, influencing the coupled air–sea system (e.g., Price et al. 2008; Dare and McBride 2011; Mei and Pasquero 2013; Wang et al. 2016). For instance, the widespread cold wake could affect the genesis and development of subsequent TCs (e.g., Brand 1971; Bender and Ginis 2000). The extensive and long-lasting cold wakes increase the probability for the later TCs passing over regions with previous TC-reduced SST and thus being suppressed, that is, a cyclone–cyclone through-ocean pathway (Balaguru et al. 2014). The cold patches left by TCs could also stabilize the atmospheric boundary layer and reduce surface wind speed several days after TC passage (Wallace et al. 1989; Xie et al. 1998; Lin et al. 2003b). On the contrary, the TC-caused anomalous warming in the subsurface ocean can persist for a much longer period of time (Pasquero and Emanuel 2008; Mei et al. 2013); in an equilibrium sate, this net ocean heat uptake (i.e., restored SST plus sustained anomalous subsurface warming) would be balanced by meridional heat transport to other latitudes and has a great potential to influence global climate (Emanuel 2001; Sriver and Huber 2007; Jansen and Ferrari 2009; Mei et al. 2013; Zhang et al. 2018; Zhang et al. 2022).

Given the important roles that cold wake plays in modulating the weather and climate system in a wide-range time scale, it is of great importance to fully characterize and understand the factors and processes governing the TC-induced SST cooling. Both observational analyses (e.g., Sanford et al. 1987; D'Asaro et al. 2007; Guan et al. 2014) and numerical experiments (e.g., Price 1981; Chiang et al. 2011) have shown that the cooling is affected by three main processes: oceanic diapycnal mixing, vertical and horizontal advection, and air–sea surface heat exchange. In cases associated with strong TCs, diapycnal mixing, principally generated by the shear instability of TC-forced near-inertial currents at the mixed layer base, accounts for around 80% of the total cooling, while upwelling and air–sea heat exchange contribute to the remaining cooling (Jacob et al. 2000; Huang et al. 2009; Vincent et al. 2012).

Generally, the magnitude of TC-induced SST cooling varies widely from less than 1°C to more than 11°C (Lin et al. 2003a; Dare and McBride 2011), owing to differences in TC attributes (including intensity, translation speed, and size) and upper-ocean stratification (Goni and Trinanes 2003; Lin et al. 2008, 2009; Mei et al. 2012, 2015b; Vincent et al. 2012; Mei and Pasquero 2013; Pun et al. 2018). Using satellite measurements, Lloyd and Vecchi (2011) composited the TC-induced SST cooling at a global scale and indicated that the SST cooling magnitude increased with TC intensity up to category 2 and saturated for TCs above category 3, confirming the inhibition effect of strong ocean stratification on TC intensification via negative feedback. Moreover, the oceanic stratification variabilities resulting from multiscale processes, such as mesoscale eddies (Shay et al. 2000) or barrier layers (Balaguru et al. 2012; Yan et al. 2017), could further modulate the magnitudes of SST cooling and TC intensification. For instance, Shay et al. (2000) elucidated that Hurricane Opal (1995) rapidly intensified from category 1 to category 4 upon encountering a warm eddy in the Gulf of Mexico and reduced SST cooling. Balaguru et al. (2012) reported that TC intensification is nearly 50% higher when passing over barrier layers, which could reduce SST cooling by restraining diapycnal mixing (Reul et al. 2014).

TC translation speed, which determines the duration of strong winds over a local point [i.e., the residence time (RT)], also plays a key role in modulating the SST cooling and the strength of negative feedback (Lin et al. 2009). Mei et al. (2012) composited the satellite-detected SST cooling and revealed that the SST cooling decreased with increasing TC translation speed, as more kinetic energy was input into the upper ocean by slower-moving TCs than faster TCs. In particular, they further demonstrated that the storm translation speed could exert an important control on its intensity via modulating the strength of negative feedback: faster-moving TCs generating less SST cooling tend to promote TC intensification.

Similar to translation speed, storm size also critically correlates with the RT and has an important potential to affect the SST cooling and subsequent TC intensification (Price 1981; Knaff et al. 2013). Theoretically, a large TC implies that winds stronger than a certain magnitude (such as gale-force wind at 34 kt; 1 kt $\approx$ 0.51 m s^{-1}) blow over a local point for a longer duration, input more energy into the ocean, inducing stronger SST cooling and negative feedback, compared to a small TC. However, the effect of storm size on TC–ocean interaction has received less attention. D'Asaro et al. (2014) examined the SST cooling induced by several TCs and revealed that typhoons with larger sizes tended to induce stronger cooling with wider spatial extension. Pun et al. (2018) demonstrated that the dramatic cooling (~7°C) left by Supertyphoon Megi (2010) in the South China Sea was mainly attributed to an abrupt size expansion. Through numerical experiments, Pun et al. (2021) assessed the influence of storm size uncertainty arising from operational TC forecasting models on simulated SST cooling. Such an uncertainty in predicted storm size was

further suggested to be of vital importance in TC intensity forecasting (Bender et al. 2017). Furthermore, Lin et al. (2021) compared the rapid intensification (RI; with intensity change larger than 30 kt over 24 h) processes of Supertyphoons Hagibis (2019) and Haiyan (2013) and found that a TC with a small size was more likely to undergo RI partially because of the weaker SST cooling it produces.

The aforementioned studies underline the vital role that storm size may play in modulating the SST cooling and negative feedback on TC intensification. However, these studies considered only a very limited number of cases. Therefore, a comprehensive study is needed to systematically examine the effect of storm size on the magnitude of SST cooling and hence the strength of ocean negative feedback onto TC intensification. In this study, we attempt to fill this gap and examine the effect of storm size on the spatiotemporal characteristics of SST cooling and negative feedback in the tropical western North Pacific (WNP), the region experiencing the most frequent and intense TCs (Webster et al. 2005; D'Asaro et al. 2011). Our results show that TCs with larger sizes tend to induce stronger SST cooling and reduced enthalpy flux, preventing TCs from intensifying. This paper is structured as follows. In section 2, we briefly describe the data and methods in use. In section 3, we comprehensively examine the effect of storm size on the magnitude, spatial extension, and temporal evolution of the TC-induced SST cooling. The dependence of TC intensification and RI on storm size is presented in section 4, and conclusions and discussion of the results are given in section 5.

2. Data and methods

a. TC best track data

TC best track data for the WNP are obtained from the International Best Track Archive for Climate Stewardship (IBTrACS; Knapp et al. 2010), distributed by the U.S. Joint Typhoon Warning Center (JTWC), which provides TC center position, 1-min sustained maximum wind speed (Vmax), and storm size at 6-h intervals. TC intensity, measured by Vmax in this study, is classified as follows: tropical depression (TD), tropical storm (TS), and the commonly used Saffir–Simpson scale categories 1–5 (abbreviated as Cat 1–5). The intensification rate (IR) of a TC, defined as the change of Vmax in the subsequent 24 h after passing the current location, is estimated to characterize TC intensity tendency. TC translation speed (Uh) is computed by dividing the sum of moving distance of TC 6 h before and 6 h after reaching the current location by 12 h.

Storm size represents the maximum radial extent of a certain wind speed magnitude (Kimball and Mulekar 2004; Pun et al. 2021) and can be characterized as wind radii of maximum wind (RMW), such as typhoon- or hurricane-force wind at 64 kt (R64), destructive-force wind at 50 kt (R50), and gale-force wind at 34 kt (R34) (Sampson et al. 2017). The TC best track data have provided 6-hourly wind radii information since 2004, with estimates in the four TC quadrants relative to the true north (Knaff and Sampson 2015; Knaff et al. 2016; Song and Klotzbach 2016). For simplicity, R34, R50, and R64 in this study are estimated as the azimuthal average of nonzero radii in the four quadrants. It should be noted that the quality control and postseason assessment of wind radii of the JTWC best track started from 2014, and thus the data quality during 2004–13 and 2014–19 may be not the same. However, although this difference of quality control certainly should be taken into account when focusing on individual TC cases, it should not significantly affect our major results of the statistical analysis here based on a large number of TC cases. An experiment only using TC cases during 2014–19 is repeated and the results are consistent with that using all TC cases during 2004–19.

b. SST observations

The optimally interpolated (OI) SST product (daily, with 0.25° × 0.25° spatial resolution) measured by satellite microwave sensors, which can penetrate clouds and provide reliable estimates of SST even under TC conditions (Wentz et al. 2000), are obtained from the Remote Sensing Systems and used to examine the TC-induced SST cooling. To be consistent with the availability of the storm size data, SST data during 2004–19 are used here. Following Mei and Pasquero (2013), the daily SST data are first preprocessed to remove the climatological seasonal cycle and long-term linear trend at each grid. For each 6-h TC track point, the residual daily SSTs within a 1000 km × 1000 km domain centered at TC center are extracted from 30 days before the TC (day −30) to 60 days afterward (day 60). The residual SSTs are then linearly interpolated onto a TC coordinate system (along- and cross-track directions) with 10 km × 10 km grids. The time series of the TC-induced SST anomaly (SSTA) is calculated by subtracting pre-TC SST (the average SST of 12 to 3 days before TC passage).

The analysis here is limited to TC track points with Vmax above TS given the fact that storm size is characterized by at least 34-kt wind radii. Moreover, considering the presence of strong meridional gradients of subsurface thermal structure in the WNP (D'Asaro et al. 2014), only TCs located equatorward of ~25°N where the mixed layer is deep are considered here to minimize the influence of lateral ocean temperature gradients and potential effects from mesoscale eddies at higher latitudes (Lin et al. 2008). Overall, a total of 452 TCs, with more than 5300 TC track points, are used in the following analysis (Fig. 1).

c. Reanalysis datasets

To augment the analysis, additional reanalysis datasets are employed. The temperature profiles in the month of TC passage are extracted to represent the pre-TC upper-ocean stratification, obtained from the monthly ORAS5 dataset during 2004–19 of the European Centre for Medium-Range Forecasts (ECMWF). The vertical wind shear (VWS), an atmosphere dynamical factor that controls TC intensification, is calculated as the 200- and 850-hPa wind difference averaged within a ring (200–800 km) from TC center (DeMaria et al. 2005; Rogers et al. 2017). We obtained the 6-h wind fields at

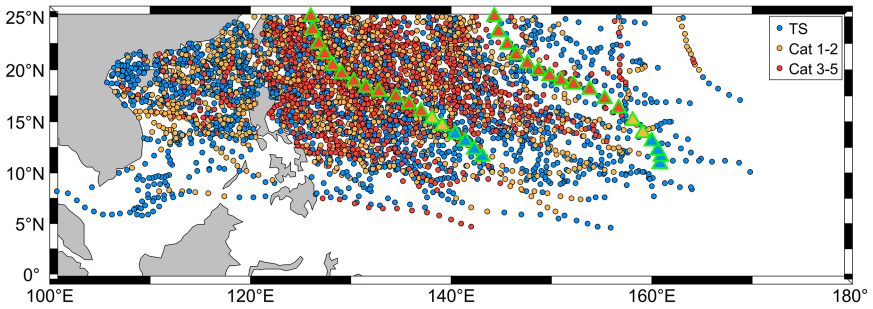

FIG. 1. Six-hourly TC track points for TS (blue), Cat 1–2 (yellow), and Cat 3–5 (red) TCs from 2004 to 2019 based on the JTWC best track dataset in the WNP. The green-edged triangles indicate the tracks of TC Neoguri (2014) and TC Lekima (2013) for case studies in section 3a.

200 and 850 hPa from the ERA5 database at each 0.25° grid during 2004–19.

To explore the effect of TC-induced SSTA on TC intensification, the enthalpy flux from ocean to TC, that is, sensible flux (Q_s) plus latent flux (Q_L), is estimated according to the bulk aerodynamic formulas (Jacob and Shay 2003)

$$Q_s = C_H V(T_s - T_a)\rho_a C_{pa} \text{ and} \tag{1}$$

$$Q_L = C_E V(q_s - q_a)\rho_a L_{va}, \tag{2}$$

where C_H and C_E are exchange coefficients of the sensible and latent heat, respectively, both of which were taken as 1.3×10^{-3} based on the observations under TC conditions; V is TC wind speed; T_s and T_a are during-TC SST and near-surface air temperature; q_s and q_a are surface and air specific humidity; and ρ_a, C_{pa}, and L_{va} are air density, heat capacity of the air, and latent heat of vaporization. For each TC track point, T_s is based on the satellite-observed SST. Note that T_a and dewpoint temperature used to calculate q_s and q_a are obtained from ERA5. Using T_a and dewpoint temperature from another dataset, the U.S. National Centers for Environmental Prediction Climate Forecast System Reanalysis (NCEP CFSR; 6-hourly, 0.5° × 0.5°), to estimate the enthalpy flux leads to the same conclusion, despite some quantitative differences in the results (not shown here).

d. Wind energy input into the upper ocean

TC-induced SST cooling is highly related to the TC forcing. Here the metric of Wind Power index (WPi) proposed by Vincent et al. (2012), which comprehensively integrates the effect of TC intensity, translation speed, and size (our focus here), is employed to characterize the TC forcing and elucidate the effect of storm size. The WPi builds on the power dissipation (PD) at sea interface by friction, a good proxy of the amount of kinetic energy transferred from the TC into the ocean which triggers the SST cooling (Emanuel 2005). The PD and WPi are calculated as

$$\mathrm{PD}(x, y) = \int_{t_o}^{t_c} \rho_a C_D(x, y, t)|V(x,y,t)|^3 dt \quad \text{and} \tag{3}$$

$$\mathrm{WPi}(x, y) = [\mathrm{PD}(x,y)/\mathrm{PD}_o]^{1/3}, \tag{4}$$

where $V(x, y, t)$ is local magnitude of wind speed, $C_D(x, y, t)$ is the local dimensionless surface drag coefficient (Large and Yeager 2009), and t_o and t_c are the time when the storm starts and stops influencing a certain location, respectively. The term $\mathrm{PD}_o = \int_{t_o}^{t_c} \rho C_D |V_o|^3 dt$ is a normalization constant corresponding to a weak storm with translation speed of 5 m s^{-1} and Vmax of 17.5 m s^{-1}.

To calculate WPi, the gridded wind field within 1000 km of the TC center is constructed using the analytical axisymmetric TC wind model proposed by Willoughby et al. (2006). The Willoughby et al. (2006) TC wind model is derived based on a large number of TC wind observations (Willoughby and Rahn 2004), whose dual-exponential profile can more accurately capture the wind speed outside the eyewall and describe the broader slow-changed annular outer regions observed in reality (Yan and Zhang 2022). The radial wind speed of the dual-exponential wind profile is as follows:

$$V_r = V_i = \mathrm{Vmax}\left(\frac{r}{\mathrm{RMW}}\right)^n, \quad (0 < r \le \mathrm{RMW}), \tag{5a}$$

$$V_r = V_i(1 - \omega) + V_o\omega, \quad (\mathrm{RMW} < r \le R_2), \tag{5b}$$

$$V_r = V_o = V_{\max}\left[(1 - A)\exp\left(-\frac{r - \mathrm{RMW}}{X_1}\right) + A\exp\left(-\frac{r - \mathrm{RMW}}{X_2}\right)\right], \quad (R_2 \le r < \infty), \tag{5c}$$

$$\omega = \frac{nX_1}{nX_1 + \mathrm{RMW}}, \tag{5d}$$

$$n = 0.406 + 0.0144V_{\max} - 0.0038\varphi, \tag{5e}$$

$$A = 0.069 + 0.0049V_{\max} - 0.0064\varphi, \tag{5f}$$

$$X_1 = 317.1 - 2.026V_{\max} + 1.915\varphi, \tag{5g}$$

where V_i and V_o are the tangential wind component inside the TC eyewall ($0 < r \le \mathrm{RMW}$) and beyond the transition zone ($R_2 \le r < \infty$) of the wind profile, and the transition zone lies at $\mathrm{RMW} < r \le R_2$; X_1 and X_2 are the fitted slower and fixed rapid exponential decay lengths in the outer vortex; n is

the exponent for the power law inside the RMW; A is the fitted contribution of the faster exponential to the wind profile; and ω is a weighted function. The distance R_2 from TC center can be each of the storm sizes (R34, R50, or R64). The X_2 is determined by substituting the calculated V_r from Eq. (5b) into Eq. (5c) when fixing $r = R_2$. Therefore, the adoption of this TC model with dual-exponential wind profile efficiently integrates the storm size information independent of RMW into the WPi.

3. Effect of TC size on sea surface cooling

In this section, the effect of storm size on TC-induced SST cooling is examined. We start with a comparison of SSTA generated by two TC cases, namely TC Lekima (2013) and TC Neoguri (2014), which have similar intensity and translation speed but substantially differ in size. We then perform composite analysis to explore the effect of storm size on the magnitude, spatial extension, and temporal evolution of the SSTA. Finally, we use the metric of WPi to uncover the mechanism by which the storm size affects SST cooling.

a. A case study

Two Cat 5 TCs passing over the WNP are selected: the compact TC Lekima in October 2013 and the large TC Neoguri in July 2014 (Fig. 2a). Lekima and Neoguri have very similar tracks and the same Vmax of 72 m s^{-1} at around 20°N. We focus on the domains within 15°–25°N (black boxes in Fig. 2a), wherein the two TCs have similar intensities (61.5 m s^{-1} for Neoguri vs 64.9 m s^{-1} for Lekima) and Uh (7.0 vs 7.5 m s^{-1}) on average (Fig. 2b) to compare the TC-generated cold wakes. The main difference is that the storm size of Neoguri is much larger than Lekima (Fig. 2c). For instance, the average R34 of Neoguri is approximately 292 km, 41% larger than that of Lekima (i.e., 207 km).

Neoguri and Lekima generated rather distinct cold wakes (Fig. 2a). Although both exhibited rightward shifts relative to TC tracks, the maximum SSTA of −6.6°C induced by Neoguri is nearly 3 times of that by Lekima (i.e., −2.4°C). The width of the cold wake, defined as the distance of positions where SSTA is −0.5°C on each side of the TC track (Mei and Pasquero 2013), is also estimated to measure the spatial extension of the cold wake. At around 20°N where maximum SSTA occurs for both TCs, the cold wake width of Neoguri is 1140 km, much larger than the 530 km of Lekima. The remarkable effect of storm size shown here is generally consistent with previous case studies (e.g., D'Asaro et al. 2014; Pun et al. 2018). Given the similar intensities and translation speeds between the two TCs, we attribute this more remarkable cold wake by Neoguri than Lekima to its larger storm size. As shown in Fig. S1 in the online supplemental material, the along-track WPi of Neoguri is about 25% larger than that of Lekima in the focused domains, which implies more kinetic energy input into the ocean to generate stronger cooling. To exclude potential contamination from pre-TC upper-ocean stratification, we performed a series of numerical experiments as in Pun et al. (2018). The results confirm that in comparison with Lekima the relatively larger size of Neoguri is indeed the dominant factor in producing a more remarkable cold wake (not shown here).

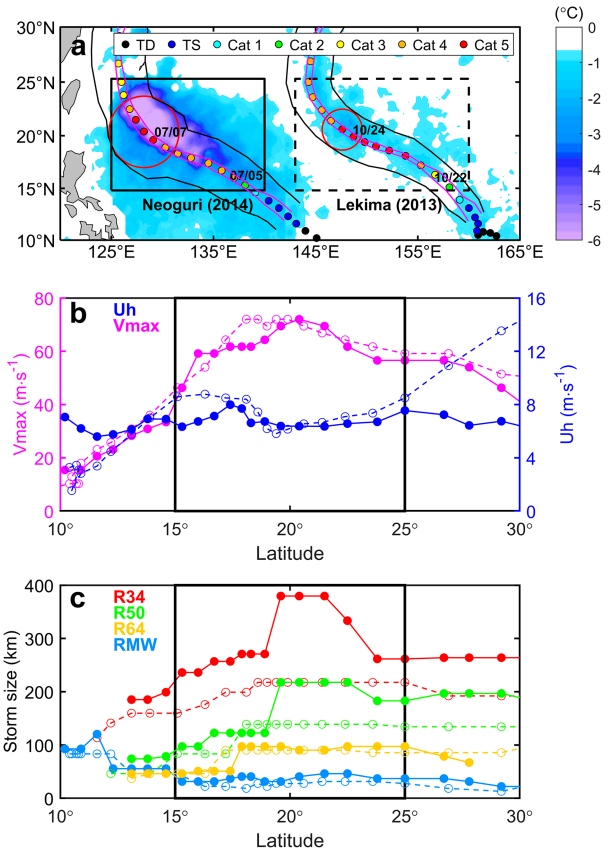

FIG. 2. Comparison of the cold wakes induced by a large versus a small TC. (a) Best tracks of TCs Neoguri (2014) (colored dots; leftward) and Lekima (2013) (colored dots; rightward), and the maximum SSTA left by the two TCs (background color), which is calculated with the minimum SST on days 0–5 post-TC minus pre-TC SST. The two TCs have nearly parallel tracks with a distance of about 2000 km, initially moving northwestward between 10° and 25°N and then turning to northward poleward of 25°N. Coincidentally, both TCs reached their lifetime peak intensity with the same Vmax of 72 m s^{-1} at around 20°N. The black and magenta solid curves along TC tracks indicate the R34 and RMW of TCs, respectively. Red cycles show the R34 (380 and 218 km for Neoguri and Lekima, respectively) when the TC centers are located around 20°N. The solid boxes indicate the focused domains. (b) TC intensity Vmax (magenta) and translation speed Uh (blue) as a function of latitude for TCs Neoguri (solid curve with closed cycles) and Lekima (dashed curve with open circles). (c) As in (b), but for storm sizes represented by RMW (blue), R64 (yellow), R50 (green), and R34 (red). The focused domains from 15° to 25°N are indicated in (b) and (c) by black solid lines.

b. Statistical dependence of SSTA on storm size

We then examine the statistical correlations between SSTA and individual wind radii (represented by RMW, R34, R50, and R64), and compare them with the correlations between SSTA and Vmax and Uh (Fig. 3). The SSTA here is defined

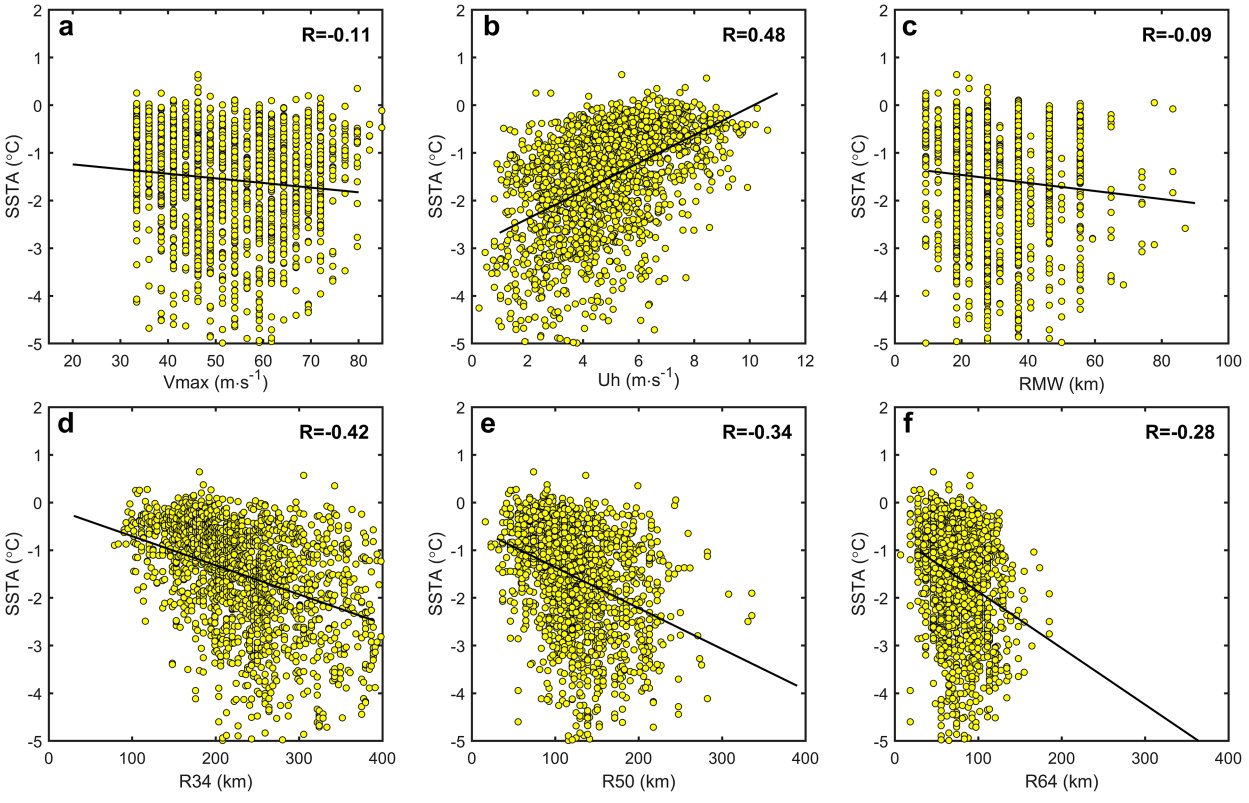

FIG. 3. Scatterplots of the SSTA averaged within 100 km of TC center on days 1–3 vs TC attributes of (a) Vmax, (b) Uh, (c) RMW, (d) R34, (e) R50 and (f) R64. The correlation coefficients R (upper-right corner) and linear regressions (black solid lines) are shown in each panel.

as the mean value of SSTA 1–3 days post-TC averaged within 100 km around TC center (i.e., approximately twice the global average RMW). Consistent with previous studies (e.g., Mei and Pasquero 2013), the SSTA increases with increasing intensity (correlation coefficient $R = -0.11$) and decreasing translation speed ($R = 0.48$) but has nearly no correlation with RMW ($R = -0.09$). The correlations between SSTA and R34, R50, and R64 are all above 0.25 and larger than that for intensity. In particular, the SSTA is most sensitive to R34 with $R = 0.42$, which is comparable to $R = 0.48$ for Uh. These calculations indicate that R34 and Uh are the top two TC parameters in affecting SSTA. The numerical experiments by Pun et al. (2021) indicate that the SSTA is more sensitive to R64 than to R34 and R50. The reasons for this inconsistency may include that 1) the SSTA in Pun et al. (2021) is defined as the maximum SSTA around TC center, while here it is defined as the average value within 100 km of TC center; 2) there is inaccuracy of model simulations in capturing the dependence of SSTA on storm size, which merits further evaluation in the future; and 3) uncertainties of R50 and R64 may be larger than R34 (Sampson et al. 2017) since estimation of wind radii in the WNP by the JTWC is mainly based on satellite observations, which is unable to accurately measure high winds. Despite this difference, both the numerical simulations of Pun et al. (2018, 2021) and our observations clearly demonstrate that the effect of storm size on SSTA is nearly as important as Uh, and thus cannot be overlooked in studying TC–ocean interactions. Hereafter, we use R34 as the representative wind radius for our analyses.

To exclude the effects of other factors, we further compare the effects of R34 and Uh on SSTA with fixed TC intensity and stratification. TC intensity is clarified into three groups (i.e., TS, Cat 1–2, and Cat 3–5). Ocean stratification is quantified by SST-T100 (Guan et al. 2021), with T100 as the average temperature in the upper 100 m (typical TC mixing depth) proposed by Price (2009). Thus, a larger SST-T100 usually indicates that the ocean stratification is conducive to larger SSTA under the same TC forcing, and vice versa. Generally, the results again show that R34 and Uh have analogous effects on SSTA, with slower-moving and larger TCs producing more dramatic SST cooling (Fig. 4). For example, for Cat 1–2 TCs with SST-T100 = 1.5°C (Fig. 4e), the SSTA synchronously increases from 0.5°C to more than 3°C when Uh decreases from 8 to 1 m s^{-1} or R34 increases from 140 to 300 km.

c. *Spatiotemporal characteristics*

The case study in section 3a shows that storm size affects not only the magnitude of the SSTA, but also its spatial structure. We then composite the SSTA averaged on days 1–3 associated with Cat 1–2 TCs, for two groups respectively with R34 smaller and larger than the mean R34 (Figs. 5a–c; Table 1). For comparison, the SSTA associated with fast- and slow-moving TCs

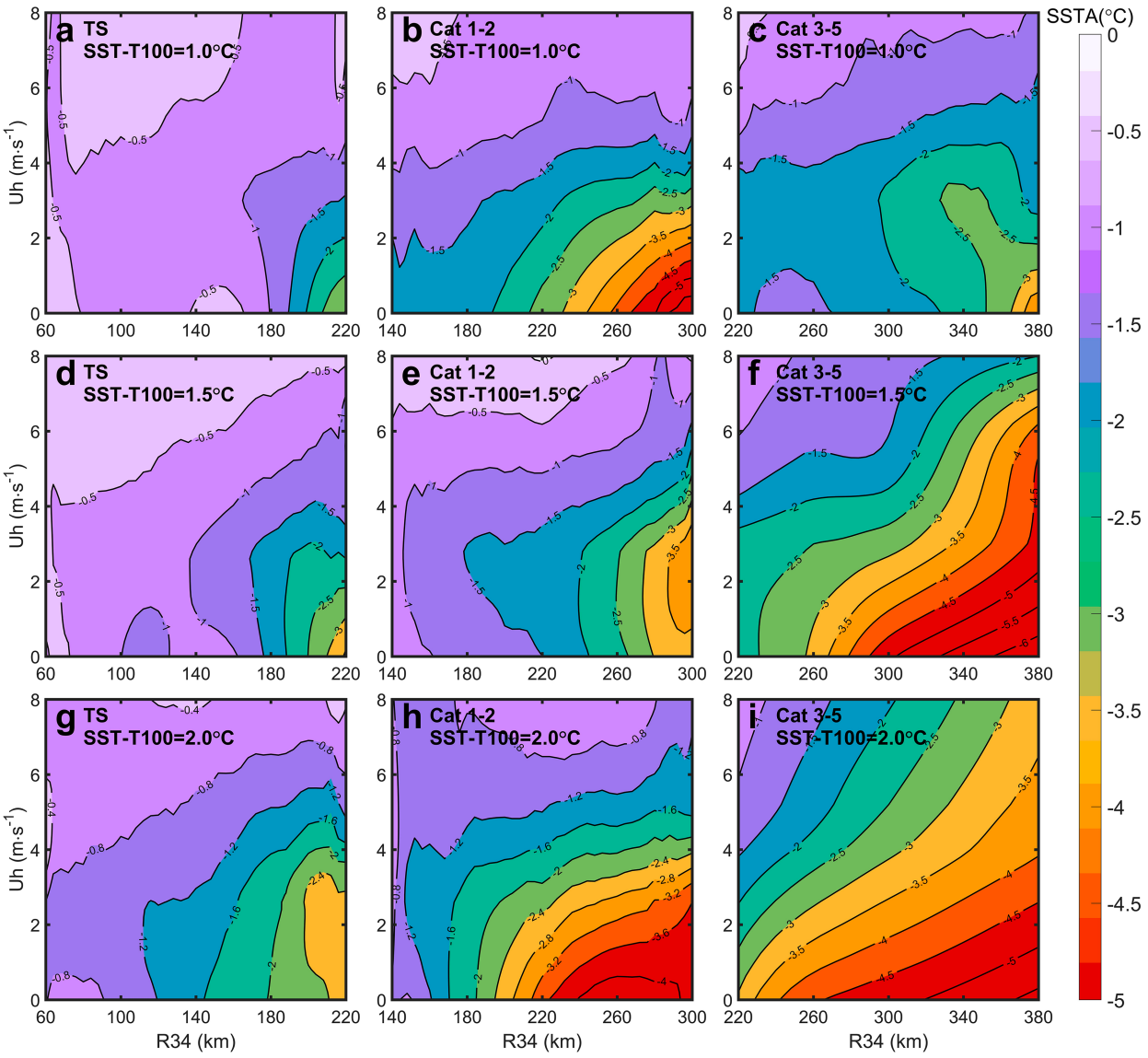

FIG. 4. SSTA as a function of Uh and R34 at fixed TC intensity and upper-ocean stratification for (a) TS, (b) Cat 1–2, and (c) Cat 3–5 TCs when SST-T100 = 1.0°C. (d)–(f),(g)–(i) As in (a)–(c), but for SST-T100 = 1.5°C and 2.0°C, respectively. The sample number for TS, Cat 1–2, and Cat 3–5 TCs is 980, 649, and 641, respectively.

are also composited (Figs. 5d–f). The mean R34 and Uh for all Cat 1–2 cases are 209 km and 4.8 m s^{-1}, respectively. The results for TS and Cat 3–5 TCs are similar and presented in Figs. S2 and S3 and Tables S1 and S2 in the online supplemental material.

As revealed in the case study, larger TCs have longer RT (and accordingly more wind energy input) and tend to induce more intense and widespread cold wake, similar to slower-moving TCs. The maximum SSTA reaches −1.9°C (−1.8°C) for large (slow-moving) TCs, but only −1.0°C (−1.0°C) for small (fast-moving) TCs. The area with SSTA stronger than −0.5°C increases by 28% with RT (defined as 2 × R34/Uh here) increasing from 18.4 to 45.9 h for slow-moving TCs in comparison with fast-moving TCs (Table 1). Compared to small TCs, the RT increases from 24.4 to 44.4 h for large TCs, and the area with SSTA < −0.5°C is nearly 3 times larger. If a linear dependence of SSTA on RT is assumed, when doubling RT the SSTA magnitude (area) would increase by −1.2°C (>300%) by merely doubling R34, significantly larger than that of −0.7°C (~25%) by merely halving Uh. This indicates that doubling storm size tends to exert a more profound effect on the cold wake than halving Uh, although both lead to a doubled RT.

Our composite results well reproduce the asymmetry of the cold wake as in the literature (e.g., Mei and Pasquero 2013), with the maximum SSTA located 60 km rightward of the TC track (Fig. 5b), mainly attributed to the fact that the clockwise rotation of wind stress on the right of track tends to resonantly strengthen the inertial currents and hence shear-induced diapycnal mixing

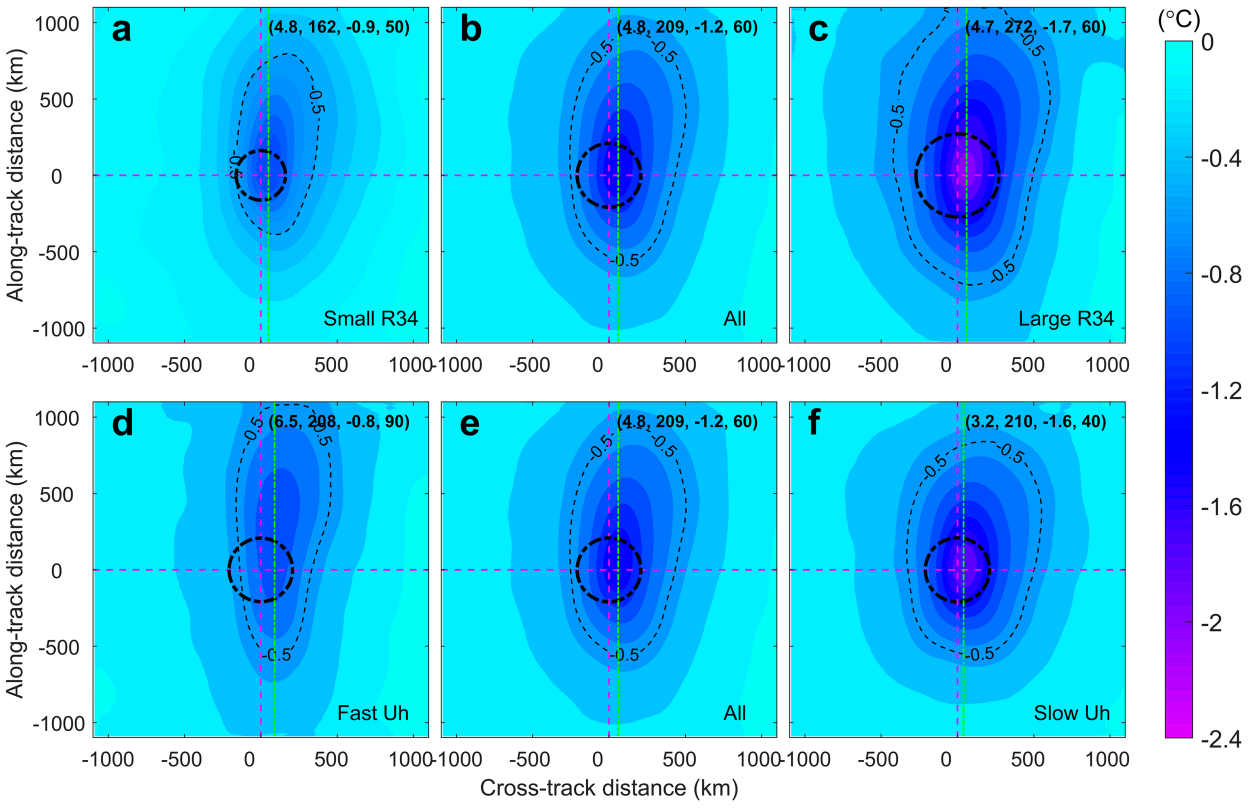

FIG. 5. Spatial pattern of composited SSTA associated with Cat 1–2 TCs in the tropical WNP. (a) Composited SSTA for compact TCs with R34 smaller than average: R34 = 209 km; (b) as in (a), but for all TC track points; (c) as in (a), but for large TCs with R34 larger than average: R34 = 209 km; (d) composited SSTA for TCs moving faster than average: Uh = 4.8 m s^{-1}; (e) as in (d), but for all TC track points; (f) as in (d), but for TCs moving slower than average: Uh = 4.8 m s^{-1}. The black dashed thick circle in each panel indicates the averaged R34. The black dashed thin line in each figure indicates the contour of SSTA = −0.5°C. The green dot–dashed line in each panel indicates the rightward shift. The numbers in parentheses in the upper-right corners indicate the average Uh, R34, SSTA averaged within 100 km around TC center, and rightward shift.

(Zhang et al. 2020). The rightward shift of the maximum SSTA increases significantly from 40 km for slow-moving TCs to 90 km for fast-moving TCs. On the contrary, the rightward shift does not considerably differ for small and large TCs (i.e., 50 vs. 60 km). Although Uh and R34 tend to modulate the RT and hence the magnitude of the SSTA in a similar manner, the difference in their effect on rightward shift can be explained as follows: when TCs move faster, the resonance of local wind and inertial current shifts farther away from TC center and thus increases the asymmetry of the SSTA, but changing storm size has much less effect on the local resonance conditions than changing Uh (Fig. S4). The moderate increase of rightward shift by expanding R34 is possibly due to the overall increase of the SSTA (Fig. 7), or likely an artifact due to the coarse resolution of satellite observations (i.e., 25 km); this merits further exploration using numerical experiments in the future.

The cold wake width increases rapidly with increasing R34 at each TC intensity (Figs. 6a–c). However, the width of the

TABLE 1. Statistics of the composited cold wakes for different R34 and Uh groups associated with Cat 1–2 TCs. The differences of related parameters between small and large TCs, or slow-moving and fast-moving TCs, are all statistically significant at the 1% level based on the Student's *t* test.

Experiment	R34 (km)	Uh (m s^{-1})	RT (h)	SSTA averaged within 100 km of TC center (°C)	Area (<−0.5°C) (×10^4 km^2)	Max SSTA (°C)	Rightward shift (km)
All	209 ± 3.4	4.8 ± 0.1	33.0 ± 1.7	−1.2	88.2	−1.4	60
Slow Uh	210 ± 4.6	3.2 ± 0.1	45.9 ± 2.9	−1.6	98.5	−1.8	40
Fast Uh	208 ± 4.9	6.5 ± 0.1	18.4 ± 0.5	−0.8	76.8	−1.0	90
Large R34	272 ± 4.0	4.7 ± 0.2	44.4 ± 3.4	−1.7	143.0	−1.9	60
Small R34	162 ± 2.0	4.8 ± 0.1	24.4 ± 1.3	−0.9	50.5	−1.0	50

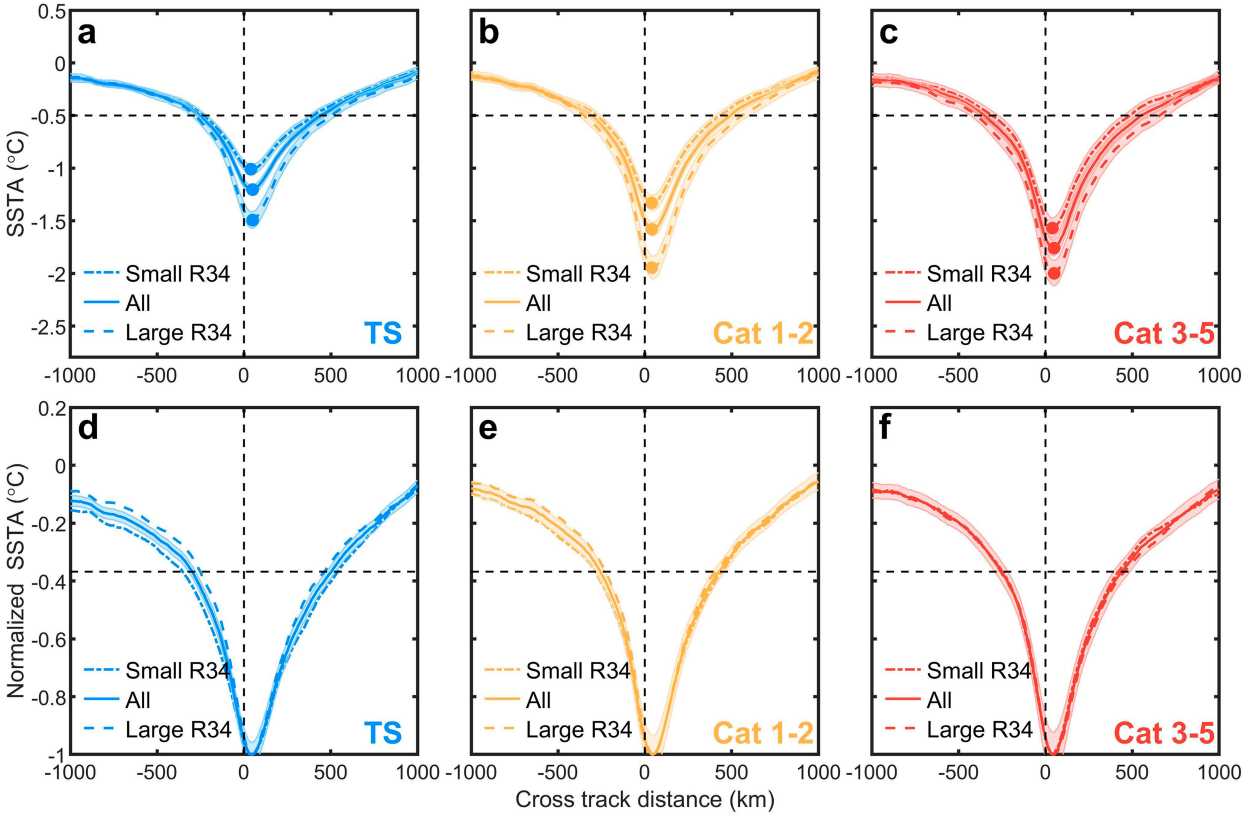

FIG. 6. Effect of TC size on the width and shape of the cold wake. (a)–(c) The SSTA as a function of cross-track distance for small (dot–dashed), all (solid), and large (dashed) R34 associated with (a) TS, (b) Cat 1–2, and (c) Cat 3–5 TCs. The horizontal black dashed lines indicate the 0.5°C cooling. The closed circle indicates the location of the maximum SSTA. (d)–(f) As in (a)–(c), but for the normalized SSTA by dividing their maximum values across track, respectively. The horizontal black dashed lines indicate the *e*-folding normalized SSTA.

normalized cold wake or the so-called shape of cold wake, defined as the distance of e^{-1} of the maximum SSTA, shows modest changes with storm size (Figs. 6d–f). For instance, the cold wake width of large Cat 1–2 (Cat 3–5) TCs widens by ~30% (33%) compared to that of compact TCs of same intensities (Fig. 6b), but for the shape, the change is about 14% (7%). This indicates that although changing storm size modulates the magnitude and spatial extension of the SSTA, the cold wake shape is quite similar. This result is based on composite analysis and may vary for individual TC cases. For example, D'Asaro et al. (2014) reported that larger TCs would result in cold wake of broader shape based on the six TC cases observed during the Impact of Typhoons on the Ocean in the Pacific (ITOP) project.

The temporal evolution of the SSTA averaged within 100 km of TC center for large and small TCs with the same TC intensity are shown in Fig. 7. Consistent with previous studies (e.g., Dare and McBride 2011; Mei and Pasquero 2013), the SST starts to drop 1–3 days before the TC passage and on average reaches its minimum on the day right after the TC passage, followed by a rapid exponential warming during the next 2 weeks and a gentle linear warming afterward. Unlike the effect of Uh on the timing of the maximum cooling, wherein slow-moving TCs generate the maximum cooling 2 days after the TC passage (Mei and Pasquero 2013), the SSTA all peak on the day right after the TC passage independent of the storm size despite the differences in the magnitude of the cooling. One plausible reason is that storm size modulates RT in a similar way as Uh but has much less effect on the resonance conditions between wind and inertial current (Fig. S4). As reported in the literature (e.g., Dare and McBride 2011), the larger SSTA induced by larger TCs would take longer time to dissipate (recover to −0.5°C here). However, the normalized SSTA manifests the same dissipation shape for all TC conditions. Following the nonlinear least squares fit to an exponential curve as Eq. (7) below (Mei and Pasquero 2013), the estimated dissipation time is approximately 10 days, regardless of TC intensity and size:

$$\mathrm{SSTA}(t) = A \exp\left(-\frac{t}{\Gamma}\right), \tag{7}$$

where t is the certain time after the TC passage when the SSTA dissipates, A is the amplitude of normalized SSTA, and Γ is the estimated dissipation time.

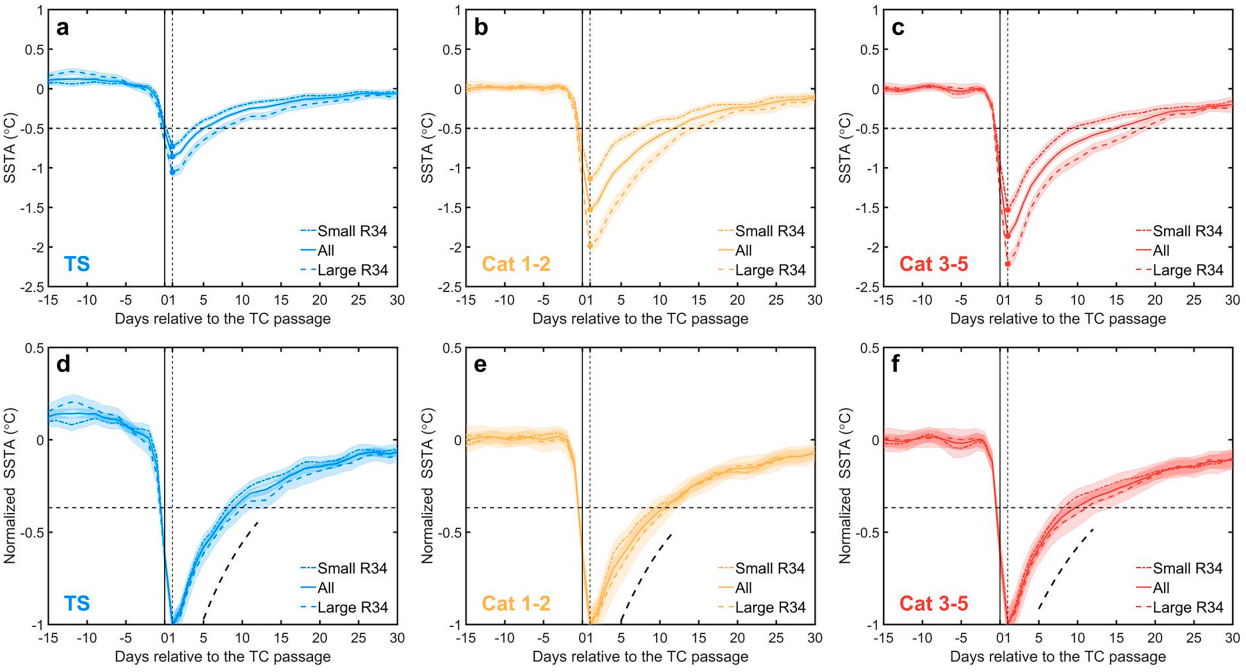

FIG. 7. Temporal evolutions of composited SSTA with different R34 for (a) TS, (b) Cat 1–2, and (c) Cat 3–5 TCs. (d)–(f) As in (a)–(c), but for normalized SSTA with respect to their maximum SSTA. The horizontal black dashed lines in (a)–(c) and (d)–(f) indicate the 0.5°C cooling and e^{-1}. Thick black dashed curves in (d)–(f) indicate the exponential function.

d. *Influence of storm size on wind energy input*

Conventionally, the effect of storm size is commonly thought to be equivalent to that of translation speed by modulating the RT of TCs' wind forcing. The above composite analysis based on satellite observations reveals that while the same increase of RT can be achieved by increasing R34 or slowing Uh, storm size appears to exert a more profound effect than translation speed on the magnitude and spatial extension of the cold wake (Figs. 5 and 6). Given the fact that SSTA is highly determined by the kinetic energy input from TC winds into the upper ocean that could be quantified by WPi and the SSTA increases monotonously with WPi (Vincent et al. 2012), in this subsection we compare the effects of R34 and Uh on WPi.

We perform idealized experiments considering three different TCs. As shown in Table 2, all three TCs have the same intensity (Vmax = 40 m s^{-1}) and RMW (50 km), moving from east to west (Fig. 8). In the control experiment (Ctl_exp), R34 is 180 km and Uh is 5 m s^{-1}. In the large-TC experiment (Lar_exp), we keep Uh unchanged but increase R34 to 360 km to double RT. In the slow-TC experiment (Slow_exp), we keep R34 unchanged but slow down Uh to 2.5 m s^{-1} to double RT as in Lar_exp. The radial wind profiles with different R34 are displayed in Fig. 8a. Although having the same winds in the inner core (from TC center to RMW), large TCs manifest a more slowly decaying wind with radius and thus stronger winds in the outer core (outward of the RMW; Rogers et al. 2013), which is expected to increase WPi. Then WPi along cross-track sections (as indicated by red and blue lines in Figs. 8b,c) are estimated for three experiments by integrating wind cube [Eqs. (3) and (4) in section 2d] from t_o to t_c and are shown in Fig. 8d. As expected, WPi in Lar_exp with large R34 and Slow_exp with small Uh are both larger than that in Ctl_exp, indicating larger wind energy input. Furthermore, WPi in Lar_exp is larger than in Slow_exp along the cross-track section, suggesting that despite having the same RT more wind energy is injected into the upper ocean in Lar_exp, exerting a stronger influence on the TC-induced SSTA. For instance, given the same RT (Table 2), WPi averaged within 180 km in Lar_exp is 21% larger than in Slow_exp (2.9 vs. 2.4); moreover, WPi averaged outwards from 180 km in Lar_exp is nearly 3 times that in Slow_exp (1.5 vs. 0.5).

TABLE 2. Design and parameters in the three idealized TC experiments for calculating and comparing WPi of TCs with different storm size and translation speed.

Experiment	Vmax (m s^{-1})	Uh (m s^{-1})	R34 (km)	RT (2 × R34/Uh) (h)	WPi averaged within R34	WPi averaged outwards from R34
Ctl_exp	40	5	180	20	1.9	0.4
Lar_exp	40	5	360	40	2.9	1.5
Slow_exp	40	2.5	180	40	2.4	0.5

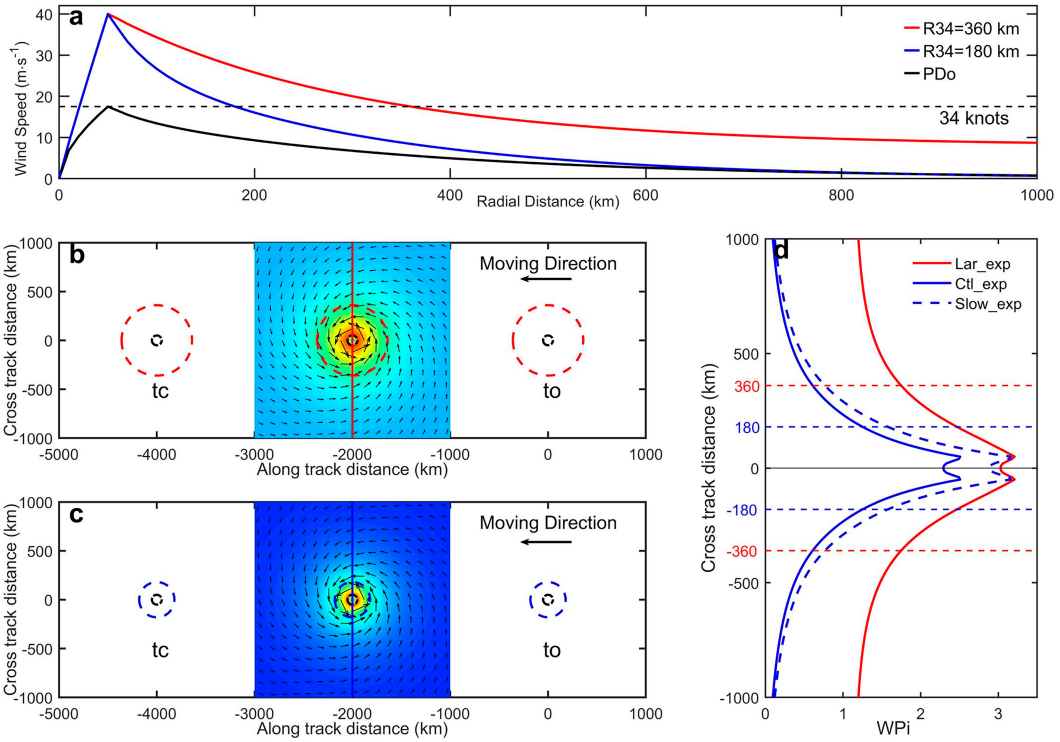

FIG. 8. (a) Constructed radial wind profiles for R34 = 180 km (blue) and 360 km (red) with the same RMW = 50 km and Vmax = 40 m s^{-1}. The wind profile for calculating PD$_o$ (black) with RMW = 50 km and Vmax = 17.5 m s^{-1} is also shown for reference. (b) Bird's-eye view of TC moving and the wind fields for Lar_exp with R34 = 360 km indicated as red dashed circles. (c) As in (b), but for the Ctl_exp and Slow_exp with R34 = 180 km. The red and blue vertical lines in (b) and (c) indicate the cross-track sections to calculate WPi. (d) WPi as a function of cross-track distance for Ctl_exp (solid blue), Slow_exp (dashed blue), and Lar_exp (red).

To quantify the dependence of SSTA magnitude (averaged within 100 km of TC center) on storm size, we further stratify TCs of same intensity into different groups based on their R34 and construct the composite for each 40-km bin. The corresponding WPi values for individual bins are calculated by assuming a constant translation speed of 5 m s^{-1}, and Vmax of 26 m s^{-1} for TS, 43 m s^{-1} for Cat 1–2 TCs, and 60 m s^{-1} for Cat 3–5 TCs. The results indicate that both SSTA and WPi show similar tendencies and increase monotonously with R34 for a given TC intensity (Fig. 9), elucidating again that TCs with larger R34 input more kinetic energy into the upper ocean and induce stronger cold wakes. We note that in Fig. 9 the SSTA induced by Cat 1–2 and 3–5 TCs nearly overlaps, and attribute this to the fact that Cat 3–5 TCs usually move faster than Cat 1–2 TCs, offsetting the effect of stronger wind forcing (Mei et al. 2012). Using same Uh indeed shows larger cooling for more intense TCs (not shown).

4. Effect of storm size on ocean cooling effect and TC intensification

As shown above, by regulating the energy input into the upper ocean, the variability of storm size significantly modulates the TC-generated SSTA. Statistically, TC IR decreases monotonically with increasing SSTA (Mei et al. 2012). Even a small increase in the SSTA magnitude could result in a large decrease of ocean's enthalpy supply and hence inhibit subsequent TC intensification. Therefore, the influences of storm size on TC intensification and rapid intensification (RI) via changes in SSTA are examined in this section.

a. Strength of the ocean cooling effect

To explore the effect of storm size, we first stratified the SSTA, enthalpy flux, and TC IR according to the TC outer-core size R34 for TS, Cat 1–2 TCs, and Cat 3–5 TCs (Figs. 9 and 10). For a fixed TC intensity, generally the bin-averaged SSTA (enthalpy flux) increases (decreases) monotonically with R34, both statistically significant at the 5% level. Correspondingly, the averaged TC IR exhibits a downward trend as R34 increases for each TC intensity group, all statistically significant at the 5% level. This is because large TCs tend to induce stronger SST cooling, which can cause a bigger reduction in the enthalpy flux from the ocean to TCs in comparison with small TCs. In addition, a large TC is usually exposed to the self-induced cooling for a longer period of time, further enhancing the ocean cooling effect and limiting the intensification of the storm. To exclude the effect on TC IR from other environmental factors, the composite processes on pre-

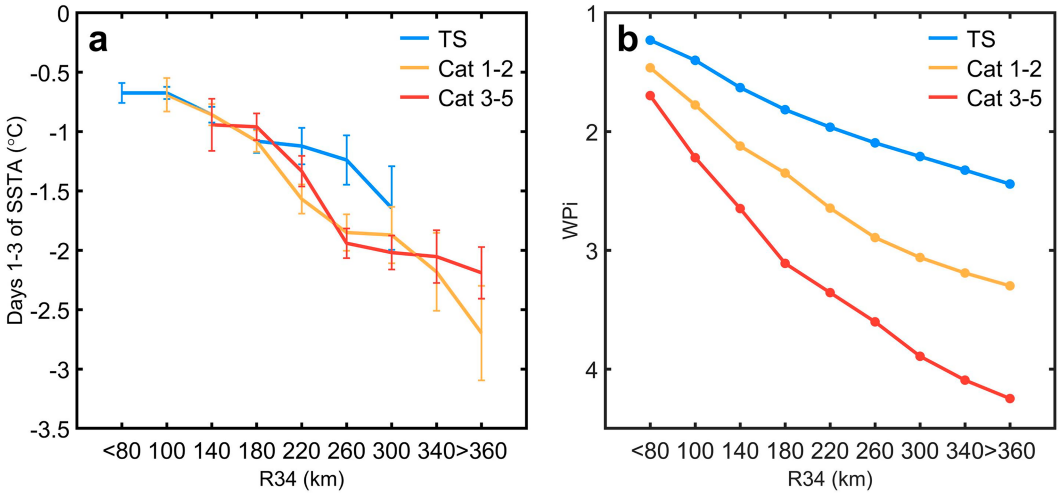

FIG. 9. (a) TC-induced SSTA averaged within 100 km of TC center as a function of R34 for TS (blue), Cat 1–2 (yellow), and Cat 3–5 TCs (red). The vertical bars indicate error bars with 95% confidence intervals. (b) WPi as a function of R34, by assuming a constant translation speed of 5 m s^{-1}, and Vmax of 26 m s^{-1} for TS (blue), 43 m s^{-1} for Cat 1–2 TCs (yellow), and 60 m s^{-1} for Cat 3–5 TCs (red). Note that the *y* ordinate is reversed.

TC SST and VWS are repeated as IR, and the results show that these two factors cannot explain the monotonic relationship between TC IR and R34 (Figs. 10c,d). Especially, VWS for Cat 1–2 and 3–5 TCs even shows decreasing trends with R34 and thus is potentially favorable for large TCs to intensify. Considering the large variability of TC outer-core size, the VWS averaged within different areas around the TC center (such as the rings of 0–500 km, 400–1000 km, or R34 to 4 × R34) are also calculated for comparison (Fig. S5) as in Rogers et al. (2017) and Lin et al. (2021), and the results are generally consistent with that in Fig. 10d.

The negative correlation between TC IR and size R34 has also been reported in previous studies (e.g., Chen et al. 2011; Carrasco et al. 2014; Xu and Wang 2015, 2018), mostly explaining this from a TC structure perspective: for large TCs higher inertial stability of the vortex in the outer core will suppress its intensification. Here we provide an alternative explanation from a TC–ocean interaction perspective: larger TCs tend to generate stronger SST cooing, in addition to longer exposure to the cooling, leading to reduced enthalpy flux (i.e., enhanced ocean cooling effect) and inhibited TC intensification. Both pathways (i.e., from either vortex dynamics or ocean cooling effect) support the observed negative correlation between IR and R34. It is worth noting that in Xu and Wang (2015, 2018), although showing a negative correlation overall, IR first increases with R34 before R34 reaches ~150 km and then decreases with R34 afterward, when averaging IR for all TC cases from TS to Cat 5. In this study, by averaging IR for fixed TC intensities, we obtain a clearly decreasing trend of IR with R34. The discrepancy may be explained as follows: IR also depends on TC intensity as revealed by Xu and Wang (2015, 2018), that is, IR first increases with intensity, peaks when Vmax is ~80 kt (~41.2 m s^{-1}, roughly corresponding to Cat 1–2 here), and then decreases with intensity afterward. In addition, R34 generally increases with TC intensity, as shown in Fig. S6, and roughly ranges between 100 and 140 km for TS and 140–180 km for Cat 1–2 TCs. Therefore, the increasing trend of IR with R34 below 150 km in Xu and Wang (2018), where TC intensity was not fixed, may be attributed to a concurrent increase of IR with intensity (also R34), which offsets the decreasing trend contributed by storm size. Furthermore, most previous studies (e.g., Carrasco et al. 2014) limited their analysis to intensifying or steady-state (i.e., IR ≥ 0) TC cases only. In this study, we consider the entire TC life cycle by further involving the decaying track points (IR < 0) to give a more comprehensive analysis, because more than 70% of Cat 3–5 TC track points tend to decay as they are approaching the maximum potential intensity (Kaplan et al. 2010). Our results show that Cat 3–5 TCs of larger sizes tend to decay more quickly than small ones (Fig. 10b).

We then divide TC cases into three groups of small (R34 smaller than 25th percentiles), medium (R34 between 25th and 75th percentiles), and large (R34 larger than 75th percentile) sizes for each TC intensity group (Fig. 11). On average, the SSTA (enthalpy flux) of small TCs is about 52% weaker (40% larger) than large TCs, and the IR is 5.2 m s^{-1} $(24\ h)^{-1}$ higher [4.3 vs −0.9 m s^{-1} $(24\ h)^{-1}$]. To examine the effect of storm size on TC intensification or decay, TC cases are further classified as intensifying (i.e., IR ≥ 0) or decaying cases (i.e., IR < 0). The results show that the average R34 sizes of intensifying TCs are about 60 km smaller than that of decaying ones, accompanied by weaker SSTA and larger enthalpy flux (Fig. 12). Our result broadens the statistical analysis of previous studies (e.g., Carrasco et al. 2014) in which only intensifying TCs with IR ≥ 0 were considered, demonstrating that large TCs either intensify more slowly or decay more quickly than small TCs. It is notable that the dependence of TC IR on R34 is more prominent for Cat 1–2 TCs than for TS or Cat 3–5 TCs (Figs. 10–12), probably because Cat 1–2 TCs are well organized and relatively far from reaching their maximum

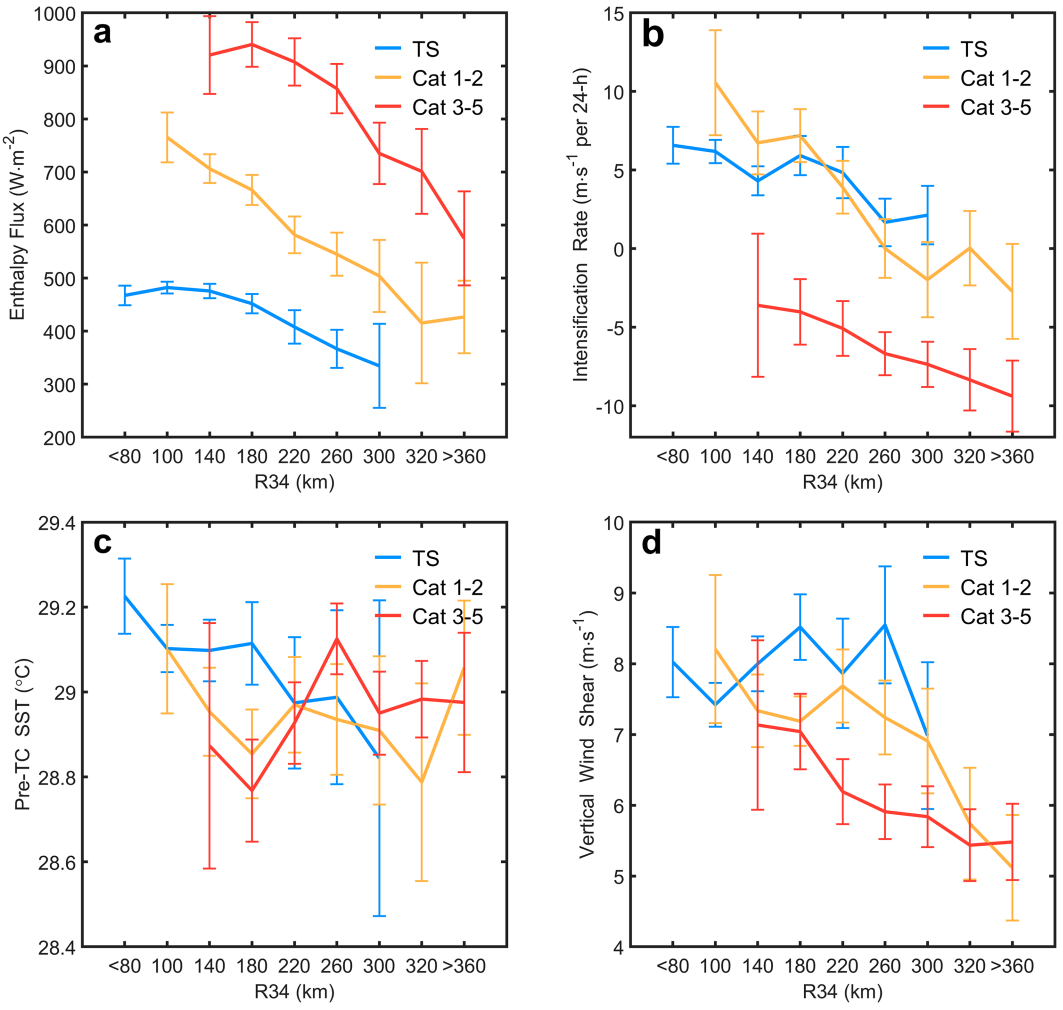

FIG. 10. Composited (a) enthalpy flux from ocean to TCs, (b) subsequent 24-h TC IR, (c) pre-TC SST averaged within 100 km of TC center, and (d) the vertical wind shear averaged within a ring of 200–800 km from TC center, as a function of R34 for TS (blue), Cat 1–2 (yellow), and 3–5 TCs (red). The vertical bars indicate error bars with 95% confidence intervals.

potential intensity (Kaplan et al. 2010) and accordingly more susceptible and sensitive to environmental factors such as the ocean cooling effect.

b. *Rapid intensification*

RI represents extreme intensification of TCs with IR larger than 30 kt (~15.4 m s^{-1}) over 24 h and is thought to be the biggest challenge in TC operational forecasting (Courtney et al. 2019). The occurrence of TC RI mostly requires a combination of multiple favorable environmental conditions and internal processes, including weak VWS, strong upper-level divergence, high pre-TC SST and ocean heat content (which helps reduce TC-induced SST cooling), fast translation speed, and small storm size (Kaplan and DeMaria 2003; Xu and Wang 2018; Shimada 2022). Carrasco et al. (2014) revealed that non-RI TCs tend to have a larger size than RI TCs and attributed this to the high outer-core inertial stability in large TCs.

In this subsection, we explore the effect of storm size on TC RI from the TC–ocean interaction perspective, by comparing R34, SSTA, and enthalpy flux between RI and non-RI (but with IR $\geq$ 0) cases for fixed TC intensities as in section 4a. In total, there are 592 RI cases in the WNP during 2004–19, accounting for 23% of all intensifying or steady-state cases analyzed here. On average, the size of TCs undergoing RI is 10%–11% smaller than that of non-RI cases, resulting in a 11%–47% weaker SSTA and 10%–23% larger enthalpy flux (Fig. 13). All the differences between RI and non-RI cases in Fig. 13 are statistically significant at least at the 10% level based on Student's t test. Taking Cat 1–2 TCs for example, R34, SSTA, and enthalpy flux of RI cases are 22 km smaller (188 vs 210 km), 0.3°C weaker (−1.1° vs −1.4°C), and 134 W m^{-2} larger (757 vs 623 W m^{-2}) than those of non-RI cases. Furthermore, when dividing TCs into two groups with small and large sizes at fixed intensity (Table 3), for small TCs with much weaker self-induced cooling effect, the probability of an

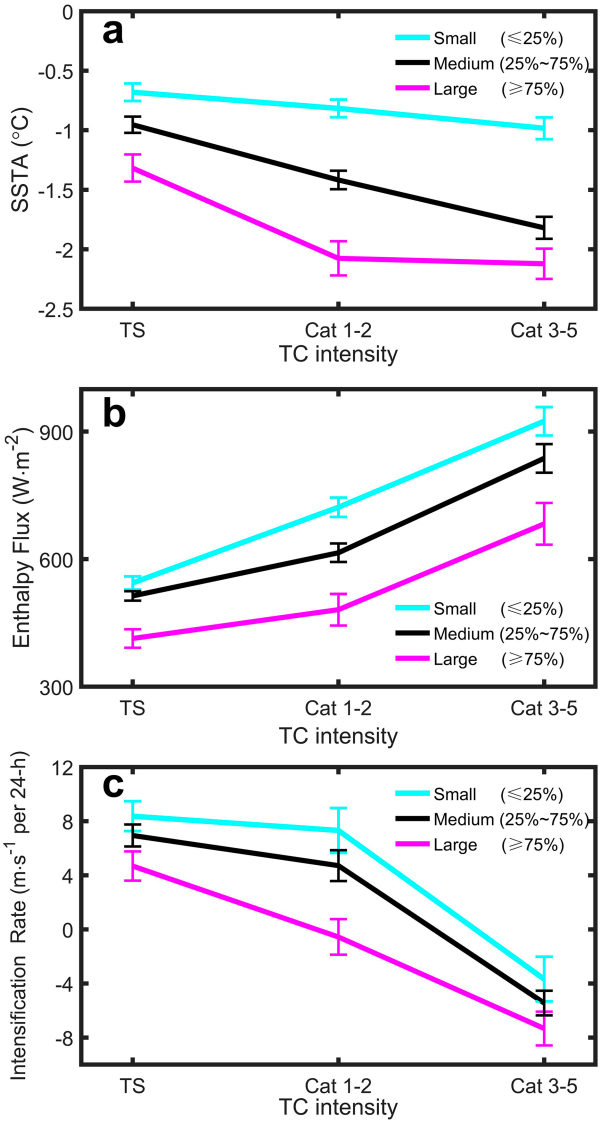

FIG. 11. Comparison of the (a) SSTA, (b) enthalpy flux, and (c) IR for groups with small (R34 smaller than its 25th percentile; cyan), medium (R34 between 25th and 75th percentiles; black), and large (R34 larger than 75th percentile; magenta) for TS, Cat 1–2, and 3–5 TCs.

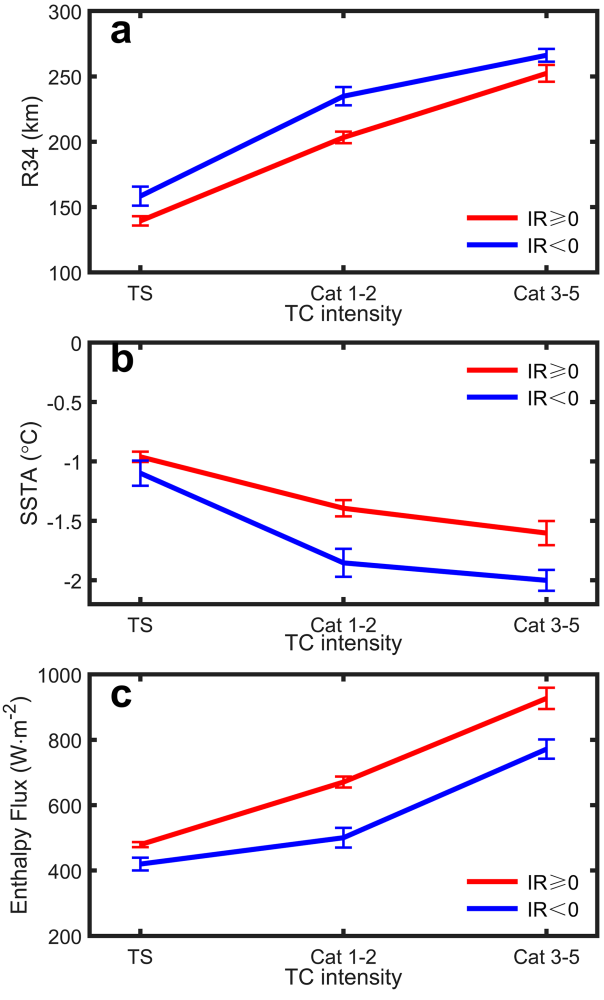

FIG. 12. Comparison of the average (a) R34, (b) SSTA, and (c) enthalpy flux for intensifying (IR ≥ 0; red) and decaying (IR < 0; blue) for TS, Cat 1–2, and 3–5 TCs. The vertical bars indicate error bars with 95% confidence intervals.

RI event is about twice of that for large TCs (e.g., 24.1% vs 12.1% for Cat 1–2 TCs).

These results suggest that TCs with smaller R34 generate weaker SSTA and consequently are fueled with larger enthalpy flux from the ocean, and thereby are more likely to experience RI. This is consistent with the case study of Lin et al. (2021), which focused on Supertyphoon Hagibis (2019). Lin et al. (2021) demonstrated that Hagibis's small size during the first stage contributed to its explosive RI (100 kt over 24 h) while the size increase during the second stage limited its further intensification because of the stronger SSTA it generated. More recently, Shimada (2022) showed that statistically small TCs could also undergo RI over waters with low ocean heat content (less than 50 kJ cm^{-2}), because the weaker SSTA they produce could offset the unfavorable subsurface ocean thermal condition. Overall, here we show that the variability in storm size can affect TC RI not only by modulating the inertial stability of the vortex, but also through the pathway of ocean cooling effect. However, it should be noted that small TCs are more likely to undergo RI, but not all small TCs will undergo RI because other favorable environmental factors are also needed for the onset of RI.

5. Conclusions and discussion

It has been long speculated that storm size may play a crucial role in regulating the cold wake induced by TCs, and this topic has been examined in several case studies (e.g., Pun et al. 2018; Lin et al. 2021). A systematic study, however, is still lacking. Through analyzing WNP TCs during 2004–19, we systematically explored the effect of storm size on TC-induced

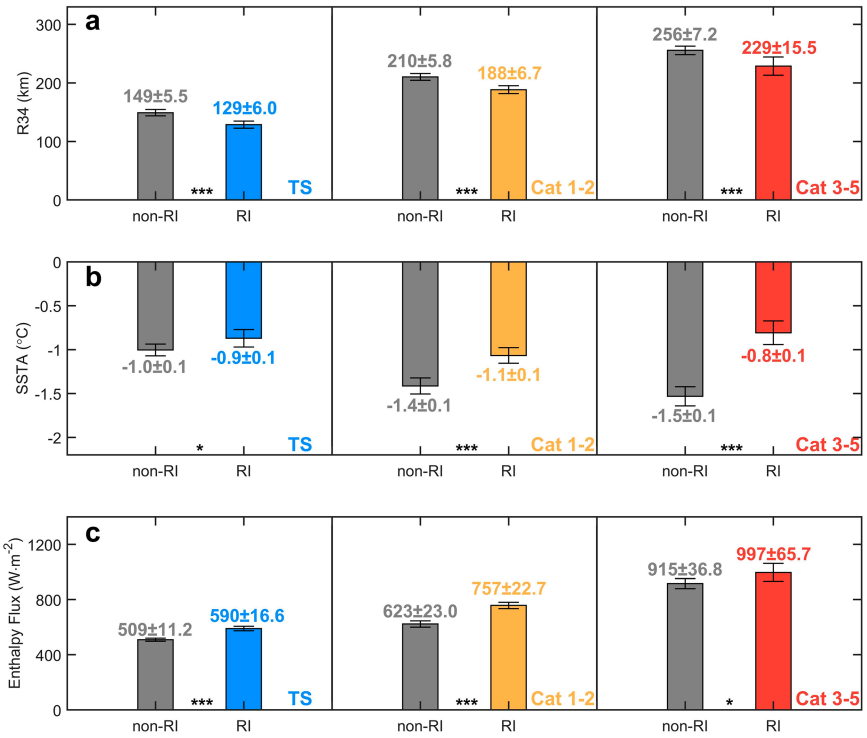

FIG. 13. Effect of storm size on rapid intensification through the pathway of ocean cooling effect. Averaged (a) R34, (b) SSTA, and (c) enthalpy flux for RI and non-RI TC cases for (left) TS, (center) Cat 1–2, and (right) Cat 3–5 TCs. For RI TCs, the average values of TS, Cat 1–2, and 3–5 TCs are indicated as blue, yellow, and red bars, and those for non-RI cases are indicated as gray bars. The black vertical bars indicate error bars with 95% confidence intervals. The mean value and its standard deviation are shown above each bar [below each bar for (b)]. The significance level for the difference between RI and non-RI cases are indicated by asterisks: * for 90%, ** for 95%, and *** for 99%.

SSTA and subsequent TC intensification. Via case study and composite analysis, the results show that large TCs tend to generate stronger and more widespread cold wake than small TCs. Typically, the average SSTA magnitude by large TC is about 90% more than small TC (taking Cat 1–2 for example, ~270 vs. 160 km for R34; 1.7° vs. 0.9°C for SSTA). The cold wake width also increases with storm size, while its shape is nearly the same for large and small TCs. Similarly, the stronger SSTA generated by large TCs would take longer time to dissipate, but the recovery shape is nearly the same with an *e*-folding time scale of around 10 days regardless of storm size. Different from the remarkable effect of translation speed on the rightward shift and timing of the maximum cooling, the effect of storm size is rather modest, probably because changing storm size has much less effect on the resonance conditions of local wind and inertial current as that by translation speed. Nevertheless, over the same increase of RT by doubling R34 or halving Uh, storm size tends to exert a more profound effect on the cold wake than Uh. Analysis of WPi shows that more wind energy is input into the upper ocean when R34 is doubled than when Uh is halved, because of a slowly decaying wind with radius in the outer core.

In practice, the nondimensional translation speed S that integrates the effects of storm size and translation speed, defined as the ratio of local inertial period ($1/f$, f is the Coriolis parameter) to RT (size/Uh), is usually employed to evaluate

TABLE 3. The average R34, SSTA, and probability of RI event for small and large TCs at fixed intensities of TS, Cat 1–2, and Cat 3–5. The differences of SSTA, R34, and RI probability between small and large TCs are all statistically significant at the 1% level based on the Student's *t* test.

	Small TCs			Large TCs		
	R34 (km)	SSTA (°C)	Probability of RI (%)	R34 (km)	SSTA (°C)	Probability of RI (%)
TS	99 ± 1.7	−0.76 ± 0.05	11.5	203 ± 5.5	−1.11 ± 0.08	6.2
Cat 1–2	160 ± 2.7	−0.96 ± 0.07	24.1	258 ± 5.4	−1.73 ± 0.11	12.1
Cat 3–5	203 ± 4.0	−1.10 ± 0.11	9.7	306 ± 6.8	−1.84 ± 0.14	4.4

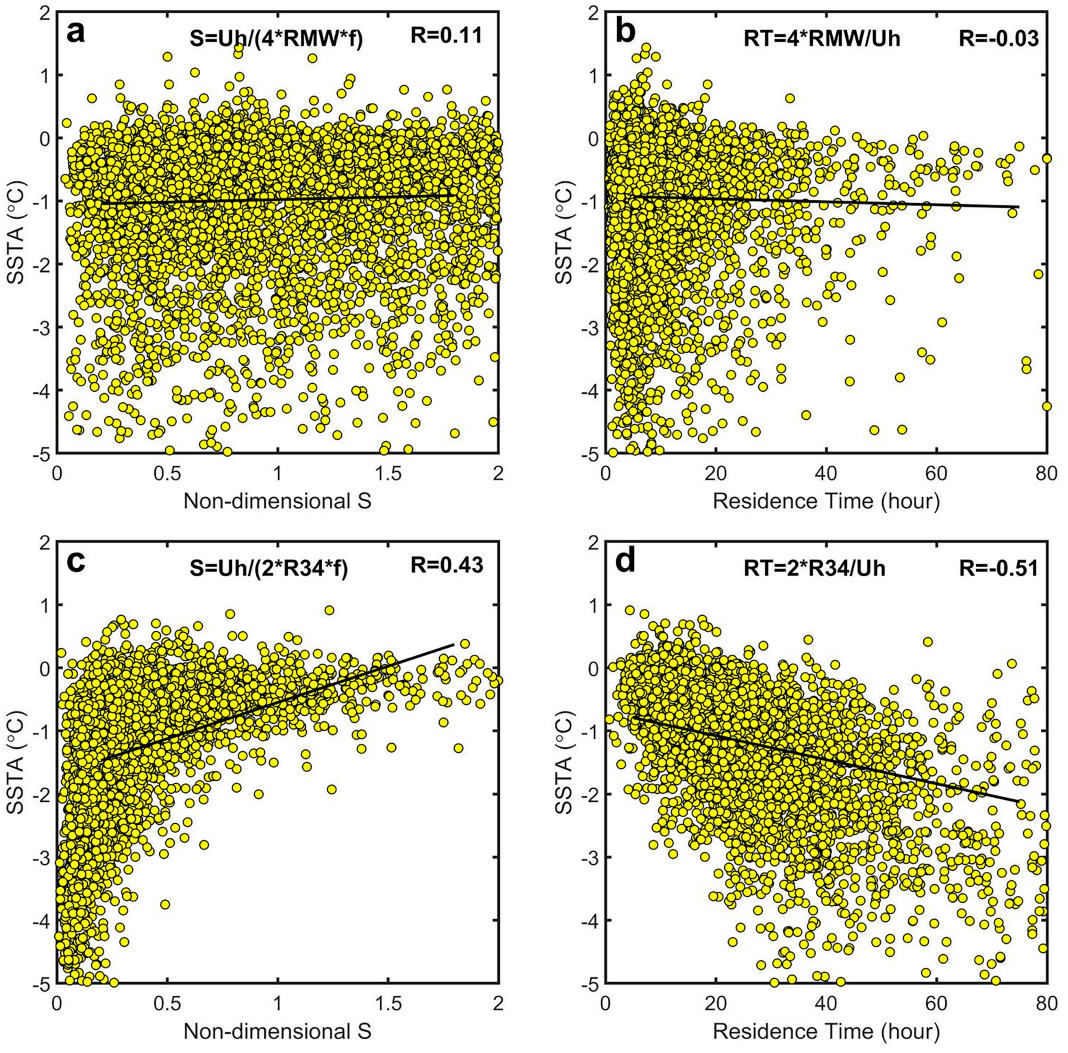

FIG. 14. Scatterplots of the average SSTA vs the nondimensional translation speed S and RT for (a) $S = \mathrm{Uh}/(2 \times \mathrm{R34} \times f)$, (b) $\mathrm{RT} = 2 \times \mathrm{R34}/\mathrm{Uh}$, (c) $S = \mathrm{Uh}/(4 \times \mathrm{RMW} \times f)$, and (d) $\mathrm{RT} = 4 \times \mathrm{RMW}/\mathrm{Uh}$. The chosen value of $4 \times$ RMW follows Price (1981). The correlation coefficients R (in the upper-right corner) and linear regressions (black lines) are shown in each panel.

the stirring effect of TC winds on the upper ocean and SSTA. However, the choice of typical storm size, usually represented by several wind radii (e.g., RMW, R64, R50, R34), is quite tricky. Intuitively, RMW is more suitable and indeed the most used (e.g., Price et al. 1994). But our statistical analysis shows that the SSTA magnitude is most sensitive to R34, with nearly no correlation with RMW. Thus, we employ R34 instead of the commonly used RMW to estimate RT and S, and examine their connections with the SSTA. Our results show that the correlations by using R34 are much larger and more significant than using RMW (Fig. 14). In particular, when incorporating R34 into S, the correlation coefficient is >0.5 and larger than that between SSTA and any single parameter of R34 or Uh, illustrating the combined effect of storm size and translation speed. These calculations suggest that R34 may be a more suitable size parameter than RMW when estimating the wind energy input into the upper ocean or studying the TC-induced cold wake.

The dependence of TC intensification and RI on storm size has been attracting much attention in the most recent decade (e.g., Rogers et al. 2013; Carrasco et al. 2014). Existing studies mainly explain negative correlation between IR and R34 from an atmospheric perspective of TC structure, in terms of inertial stability occurring in the inner core or outer core (Pendergrass and Willoughby 2009). Via case study, Lin et al. (2021) pointed out that storm size can influence TC intensification via the ocean cooling effect. Through composite analysis of a large-amount TC cases, our study further demonstrates this oceanic pathway: large TCs tend to induce stronger SST cooling and be exposed to the self-induced cooling for a longer period of time, both of which reduce enthalpy supply for the storm development and lead to weaker IR and low probability of RI. When TC intensity

is fixed, the SSTA, enthalpy flux, and IR all manifest monotonic relationships with R34, all statistically significant at the 5% level. Fueled by a ~50% weaker SSTA, small TCs have nearly twice the probability to undergo RI than large TCs (24.1% vs 12.1% for Cat 1–2 TCs). Our results add new knowledge to our understanding of the pathways via which storm size affects TC intensification.

In short, our study highlights the crucial role that storm size plays in regulating sea surface cooling and TC intensification. We argue that in any attempts to examine the TC-induced cold wake and its effect on heat redistribution within the climate system, storm size needs to be as accurately specified as other previously well-recognized TC characteristics, such as intensity and translation speed. Our results further suggest that progress in predicting storm size should lead to improved TC intensity prediction by more accurately capturing the ocean cooling effect or inertial stability. Indeed, a pioneering work by Bender et al. (2017) has shown the great potential of using regional coupled forecasting models to reliably forecast TC intensity and RI by properly specifying storm size R34. Yet, the complex interactions due to the presence of multiple pathways need to be systematically investigated via employing high-resolution coupled atmosphere–ocean models in the future. Moreover, an accurate specification and prediction of storm size can also be beneficial to forecasting and early warning of storm surges (Li et al. 2020) and heavy rainfall (Emanuel 2017), providing emergency managers with additional information to assess the damage potential of landfalling TCs.

Acknowledgments. This research was jointly supported by the 2022 Research Program of Sanya Yazhou Bay Science and Technology City (Grant SKIC-2022-01-001), the National Science Foundation of China (Grants 41876011, 92258301, 91958205), the National Key Research and Development Program (2022YFC3104304), the Hainan Province Science and Technology Special Fund (Grant ZDYF2021SHFZ265), the open research cruise NORC2021-05 supported by NSFC Shiptime Sharing Project (project number 42049905), and the Fundamental Research Funds for the Central Universities (Grants 202001013129 and 1901013184).

Data availability statement. The TC best track data are provided by the International Best Track Archive for Climate Stewardship (IBTrACS) (https://www.ncei.noaa.gov/products/international-best-track-archive). The SST data sponsored by the NASA Earth Science REASNN DISCOVER Project are obtained from REMSS (http://www.remss.com/). The temperature profile, air temperature, dew point temperature, and 200- and 850-hPa wind speed datasets are available from the European Centre for Medium-Range Forecasts (ECMWF) (https://cds.climate.copernicus.eu/cdsapp#!/dataset/).

REFERENCES

Balaguru, K., P. Chang, R. Saravanan, L. R. Leung, Z. Xu, M. Li, and J.-S. Hsieh, 2012: Ocean barrier layers' effect on tropical cyclone intensification. *Proc. Natl. Acad. Sci. USA*, **109**, 14 343–14 347, https://doi.org/10.1073/pnas.1201364109.

——, S. Taraphdar, L. R. Leung, G. R. Foltz, and J. A. Knaff, 2014: Cyclone-cyclone interactions through the ocean pathway. *Geophys. Res. Lett.*, **41**, 6855–6862, https://doi.org/10.1002/2014GL061489.

Bender, M. A., and I. Ginis, 2000: Real-case simulations of hurricane–ocean interaction using a high-resolution coupled model: Effects on hurricane intensity. *Mon. Wea. Rev.*, **128**, 917–946, https://doi.org/10.1175/1520-0493(2000)128<0917:RCSOHO>2.0.CO;2.

——, T. P. Marchok, C. Sampson, J. A. Knaff, and M. J. Morin, 2017: Impact of storm size on prediction of storm track and intensity using the 2016 operational GFDL hurricane model. *Wea. Forecasting*, **32**, 1491–1508, https://doi.org/10.1175/WAF-D-16-0220.1.

Brand, S., 1971: The effects on a tropical cyclone of cooler surface waters due to upwelling and mixing produced by a prior tropical cyclone. *J. Appl. Meteor.*, **10**, 865–874, https://doi.org/10.1175/1520-0450(1971)010<0865:TEOATC>2.0.CO;2.

Carrasco, C. A., C. W. Landsea, and Y.-L. Lin, 2014: The influence of tropical cyclone size on its intensification. *Wea. Forecasting*, **29**, 582–590, https://doi.org/10.1175/WAF-D-13-00092.1.

Chen, D. Y.-C., K. K. W. Cheung, and C.-S. Lee, 2011: Some implications of core regime wind structures in western North Pacific tropical cyclones. *Wea. Forecasting*, **26**, 61–75, https://doi.org/10.1175/2010WAF2222420.1.

Chiang, T.-L., C.-R. Wu, and L.-Y. Oey, 2011: Typhoon Kai-Tak: An ocean's perfect storm. *J. Phys. Oceanogr.*, **41**, 221–233, https://doi.org/10.1175/2010JPO4518.1.

Cione, J. J., and E. W. Uhlhorn, 2003: Sea surface temperature variability in hurricanes: Implications with respect to intensity change. *Mon. Wea. Rev.*, **131**, 1783–1796, https://doi.org/10.1175//2562.1.

Courtney, J. B., and Coauthors, 2019: Operational perspectives on tropical cyclone intensity change. Part II: Forecasts by operational agencies. *Trop. Cyclone Res. Rev.*, **8**, 226–239, https://doi.org/10.1016/j.tcrr.2020.01.003.

Dare, R. A., and J. L. McBride, 2011: Sea surface temperature response to tropical cyclones. *Mon. Wea. Rev.*, **139**, 3798–3808, https://doi.org/10.1175/MWR-D-10-05019.1.

D'Asaro, E. A., T. B. Sanford, P. P. Niiler, and E. J. Terrill, 2007: Cold wake of Hurricane Frances. *Geophys. Res. Lett.*, **34**, L15609, https://doi.org/10.1029/2007GL030160.

——, and Coauthors, 2011: Typhoon-ocean interaction in the western North Pacific: Part 1. *Oceanography*, **24**, 24–31, https://doi.org/10.5670/oceanog.2011.91.

——, and Coauthors, 2014: Impact of typhoons on the ocean in the Pacific. *Bull. Amer. Meteor. Soc.*, **95**, 1405–1418, https://doi.org/10.1175/BAMS-D-12-00104.1.

DeMaria, M., M. Mainelli, L. K. Shay, J. A. Knaff, and J. Kaplan, 2005: Further improvements to the Statistical Hurricane Intensity Prediction Scheme (SHIPS). *Wea. Forecasting*, **20**, 531–543, https://doi.org/10.1175/WAF862.1.

Emanuel, K. A., 1999: Thermodynamic control of hurricane intensity. *Nature*, **401**, 665–669, https://doi.org/10.1038/44326.

——, 2001: Contribution of tropical cyclones to meridional heat transport by the oceans. *J. Geophys. Res.*, **106**, 14 771–14 781, https://doi.org/10.1029/2000JD900641.

——, 2003: Tropical cyclones. *Annu. Rev. Earth Planet. Sci.*, **31**, 75–104, https://doi.org/10.1146/annurev.earth.31.100901.141259.

——, 2005: Increasing destructiveness of tropical cyclones over the past 30 years. *Nature*, **436**, 686–688, https://doi.org/10.1038/nature03906.

——, 2017: Assessing the present and future probability of Hurricane Harvey's rainfall. *Proc. Natl. Acad. Sci. USA*, **114**, 12 681–12 684, https://doi.org/10.1073/pnas.1716222114.

——, C. DesAutels, C. Holloway, and R. Korty, 2004: Environmental control of tropical cyclone intensity. *J. Atmos. Sci.*, **61**, 843–858, https://doi.org/10.1175/1520-0469(2004)061<0843:ECOTCI>2.0.CO;2.

Goni, G. J., and J. A. Trinanes, 2003: Ocean thermal structure monitoring could aid in the intensity forecast of tropical cyclones. *Eos, Trans. Amer. Geophys. Union*, **84**, 573–578, https://doi.org/10.1029/2003EO510001.

——, and Coauthors, 2009: Applications of satellite-derived ocean measurements to tropical cyclone intensity forecasting. *Oceanography*, **22**, 190–197, https://doi.org/10.5670/oceanog.2009.78.

Guan, S., W. Zhao, J. Huthnance, J. Tian, and J. Wang, 2014: Observed upper ocean response to Typhoon Megi (2010) in the northern South China Sea. *J. Geophys. Res. Oceans*, **119**, 3134–3157, https://doi.org/10.1002/2013JC009661.

——, and Coauthors, 2021: Tropical cyclone-induced sea surface cooling over the Yellow Sea and Bohai Sea in the 2019 Pacific typhoon season. *J. Mar. Syst.*, **217**, 103509, https://doi.org/10.1016/j.jmarsys.2021.103509.

Huang, P., T. B. Sanford, and J. Imberger, 2009: Heat and turbulent kinetic energy budgets for surface layer cooling induced by the passage of Hurricane Frances (2004). *J. Geophys. Res.*, **114**, C12023, https://doi.org/10.1029/2009JC005603.

Jacob, S. D., and L. K. Shay, 2003: The role of oceanic mesoscale features on the tropical cyclone-induced mixed layer response: A case study. *J. Phys. Oceanogr.*, **33**, 649–676, https://doi.org/10.1175/1520-0485(2003)33<649:TROOMF>2.0.CO;2.

——, ——, A. J. Mariano, and P. G. Black, 2000: The 3D oceanic mixed layer response to Hurricane Gilbert. *J. Phys. Oceanogr.*, **30**, 1407–1429, https://doi.org/10.1175/1520-0485(2000)030<1407:TOMLRT>2.0.CO;2.

Jansen, M., and R. Ferrari, 2009: Impact of the latitudinal distribution of tropical cyclones on ocean heat transport. *Geophys. Res. Lett.*, **3**, L06604, https://doi.org/10.1029/2008GL036796.

Kaplan, J., and M. DeMaria, 2003: Large-scale characteristics of rapidly intensifying tropical cyclones in the North Atlantic basin. *Wea. Forecasting*, **18**, 1093–1108, https://doi.org/10.1175/1520-0434(2003)018<1093:LCORIT>2.0.CO;2.

——, ——, and J. A. Knaff, 2010: A revised tropical cyclone rapid intensification index for the Atlantic and eastern North Pacific basins. *Wea. Forecasting*, **25**, 220–241, https://doi.org/10.1175/2009WAF2222280.1.

Kimball, S. K., and M. S. Mulekar, 2004: A 15-year climatology of North Atlantic tropical cyclones. Part I: Size parameters. *J. Climate*, **17**, 3555–3575, https://doi.org/10.1175/1520-0442(2004)017<3555:AYCONA>2.0.CO;2.

Knaff, J. A., and C. R. Sampson, 2015: After a decade are Atlantic tropical cyclone gale force wind radii forecasts now skillful? *Wea. Forecasting*, **30**, 702–709, https://doi.org/10.1175/WAF-D-14-00149.1.

——, M. DeMaria, C. R. Sampson, J. E. Peak, J. Cummings, and W. H. Schubert, 2013: Upper oceanic energy response to tropical cyclone passage. *J. Climate*, **26**, 2631–2650, https://doi.org/10.1175/JCLI-D-12-00038.1.

——, C. J. Slocum, K. D. Musgrave, C. R. Sampson, and B. R. Strahl, 2016: Using routinely available information to estimate tropical cyclone wind structure. *Mon. Wea. Rev.*, **144**, 1233–1247, https://doi.org/10.1175/MWR-D-15-0267.1.

Knapp, K. R., M. C. Kruk, D. H. Levinson, H. J. Diamond, and C. J. Neumann, 2010: The International Best Track Archive for Climate Stewardship (IBTrACS) unifying tropical cyclone data. *Bull. Amer. Meteor. Soc.*, **91**, 363–376, https://doi.org/10.1175/2009BAMS2755.1.

Korty, R. L., K. A. Emanuel, and J. R. Scott, 2008: Tropical cyclone-induced upper-ocean mixing and climate: Application to equable climates. *J. Climate*, **21**, 638–654, https://doi.org/10.1175/2007JCLI1659.1.

Large, W. G., and S. G. Yeager, 2009: The global climatology of an interannually varying air-sea flux data set. *Climate Dyn.*, **33**, 341–364, https://doi.org/10.1007/s00382-008-0441-3.

Leipper, D. F., 1967: Observed ocean conditions and Hurricane Hilda, 1964. *J. Atmos. Sci.*, **24**, 182–186, https://doi.org/10.1175/1520-0469(1967)024<0182:OOCAHH>2.0.CO;2.

Li, A., S. Guan, D. Mo, Y. Hou, X. Hong, and Z. Liu, 2020: Modeling wave effects on storm surge from different typhoon intensities and sizes in the South China Sea. *Estuarine Coastal Shelf Sci.*, **235**, 106551, https://doi.org/10.1016/j.ecss.2019.106551.

Lin, I.-I., and Coauthors, 2003a: New evidence for enhanced ocean primary production triggered by tropical cyclone. *Geophys. Res. Lett.*, **30**, 1718, https://doi.org/10.1029/2003GL017141.

——, W. T. Liu, C.-C. Wu, J. C. H. Chiang, and C.-H. Sui, 2003b: Satellite observations of modulation of surface winds by typhoon-induced upper ocean cooling. *Geophys. Res. Lett.*, **30**, 1131, https://doi.org/10.1029/2002GL015674.

——, C.-C. Wu, I.-F. Pun, and D.-S. Ko, 2008: Upper-ocean thermal structure and the western North Pacific category 5 typhoons. Part I: Ocean features and the category 5 typhoons' intensification. *Mon. Wea. Rev.*, **136**, 3288–3306, https://doi.org/10.1175/2008MWR2277.1.

——, I.-F. Pun, and C.-C. Wu, 2009: Upper-ocean thermal structure and the western North Pacific category 5 typhoons. Part II: Dependence on translation speed. *Mon. Wea. Rev.*, **137**, 3744–3757, https://doi.org/10.1175/2009MWR2713.1.

——, and Coauthors, 2013: An ocean coupling potential intensity index for tropical cyclones. *Geophys. Res. Lett.*, **40**, 1878–1882, https://doi.org/10.1002/grl.50091.

——, and Coauthors, 2021: A tale of two rapidly intensifying supertyphoons: Hagibis (2019) and Haiyan (2013). *Bull. Amer. Meteor. Soc.*, **102**, E1645–E1664, https://doi.org/10.1175/BAMS-D-20-0223.1.

Lloyd, I. D., and G. A. Vecchi, 2011: Observational evidence for oceanic controls on hurricane intensity. *J. Climate*, **24**, 1138–1153, https://doi.org/10.1175/2010JCLI3763.1.

Mei, W., and C. Pasquero, 2013: Spatial and temporal characterization of sea surface temperature response to tropical cyclones. *J. Climate*, **26**, 3745–3765, https://doi.org/10.1175/JCLI-D-12-00125.1.

——, ——, and F. Primeau, 2012: The effect of translation speed upon the intensity of tropical cyclones over the tropical ocean. *Geophys. Res. Lett.*, **39**, L07801, https://doi.org/10.1029/2011GL050765.

——, F. Primeau, J. C. McWilliams, and C. Pasquero, 2013: Sea surface height evidence for long-term warming effects of tropical cyclones on the ocean. *Proc. Natl. Acad. Sci. USA*, **110**, 15 207–15 210, https://doi.org/10.1073/pnas.1306753110.

——, S.-P. Xie, F. Primeau, J. C. McWilliams, and C. Pasquero, 2015a: Northwestern Pacific typhoon intensity controlled by changes in ocean temperatures. *Sci. Adv.*, **1**, e1500014, https://doi.org/10.1126/sciadv.1500014.

——, C.-C. Lien, I.-I. Lin, and S.-P. Xie, 2015b: Tropical cyclone-induced ocean response: A comparative study of the South

China Sea and tropical northwest Pacific. *J. Climate*, **28**, 5952–5968, https://doi.org/10.1175/JCLI-D-14-00651.1.

Pasquero, C., and K. A. Emanuel, 2008: Tropical cyclones and transient upper-ocean warming. *J. Climate*, **21**, 149–162, https://doi.org/10.1175/2007JCLI1550.1.

Pendergrass, A. G., and H. E. Willoughby, 2009: Diabatically induced secondary flows in tropical cyclones. Part I: Quasi-steady forcing. *Mon. Wea. Rev.*, **137**, 805–821, https://doi.org/10.1175/2008MWR2657.1.

Price, J. F., 1981: Upper ocean response to a hurricane. *J. Phys. Oceanogr.*, **11**, 153–175, https://doi.org/10.1175/1520-0485(1981)011<0153:UORTAH>2.0.CO;2.

——, 2009: Metrics of hurricane-ocean interaction: Vertically-integrated or vertically-averaged ocean temperature? *Ocean Sci.*, **5**, 351–368, https://doi.org/10.5194/os-5-351-2009.

——, T. B. Sanford, and G. Z. Forristall, 1994: Forced stage response to a moving hurricane. *J. Phys. Oceanogr.*, **24**, 233–260, https://doi.org/10.1175/1520-0485(1994)024<0233:FSRTAM>2.0.CO;2.

——, J. Morzel, and P. P. Niiler, 2008: Warming of SST in the cool wake of a moving hurricane. *J. Geophys. Res.*, **113**, C07010, https://doi.org/10.1029/2007JC004393.

Pun, I.-F., Y.-T. Chang, I.-I. Lin, T. Y. Tang, and R.-C. Lien, 2011: Typhoon-ocean interaction in the western North Pacific: Part 2. *Oceanography*, **24**, 32–41, https://doi.org/10.5670/oceanog.2011.92.

——, I.-I. Lin, C.-C. Lien, and C.-C. Wu, 2018: Influence of the size of supertyphoon Megi (2010) on SST cooling. *Mon. Wea. Rev.*, **146**, 661–677, https://doi.org/10.1175/MWR-D-17-0044.1.

——, J. A. Knaff, and C. R. Sampson, 2021: Uncertainty of tropical cyclone wind radii on sea surface temperature cooling. *J. Geophys. Res. Atmos.*, **126**, e2021JD034857, https://doi.org/10.1029/2021JD034857.

Reul, N., Y. Quilfen, B. Chapron, S. Fournier, V. Kudryavtsev, and R. Sabia, 2014: Multisensor observations of the Amazon-Orinoco river plume interactions with hurricanes. *J. Geophys. Res. Oceans*, **119**, 8271–8295, https://doi.org/10.1002/2014JC010107.

Rogers, R., P. Reasor, and S. Lorsolo, 2013: Airborne Doppler observations of the inner-core structural differences between intensifying and steady-state tropical cyclones. *Mon. Wea. Rev.*, **141**, 2970–2991, https://doi.org/10.1175/MWR-D-12-00357.1.

——, and Coauthors, 2017: Re-writing the tropical record books: The extraordinary intensification of Hurricane Patricia. *Bull. Amer. Meteor. Soc.*, **98**, 2091–2112, https://doi.org/10.1175/BAMS-D-16-0039.1.

Sampson, C. R., E. M. Fukada, J. A. Knaff, B. R. Strahl, M. J. Brennan, and T. Marchok, 2017: Tropical cyclone gale wind radii estimates for the western North Pacific. *Wea. Forecasting*, **32**, 1029–1040, https://doi.org/10.1175/WAF-D-16-0196.1.

Sanford, T. B., P. G. Black, J. R. Haustein, J. W. Fenney, G. Z. Forristall, and J. F. Price, 1987: Ocean response to hurricanes. Part I: Observations. *J. Phys. Oceanogr.*, **17**, 2065–2083, https://doi.org/10.1175/1520-0485(1987)017<2065:ORTAHP>2.0.CO;2.

Schade, L. R., 2000: Tropical cyclone intensity and sea surface temperature. *J. Atmos. Sci.*, **57**, 3122–3130, https://doi.org/10.1175/1520-0469(2000)057<3122:TCIASS>2.0.CO;2.

Shay, L. K., G. J. Goni, and P. G. Black, 2000: Effects of a warm oceanic feature on Hurricane Opal. *Mon. Wea. Rev.*, **128**, 1366–1383, https://doi.org/10.1175/1520-0493(2000)128<1366:EOAWOF>2.0.CO;2.

Shen, W., and I. Ginis, 2003: Effects of surface heat flux-induced sea surface temperature changes on tropical cyclone intensity. *Geophys. Res. Lett.*, **30**, 1933, https://doi.org/10.1029/2003GL017878.

Shimada, U., 2022: Variability of environmental conditions for tropical cyclone rapid intensification in the western North Pacific. *J. Climate*, **35**, 4437–4454, https://doi.org/10.1175/JCLI-D-21-0751.1.

Song, J., and P. J. Klotzbach, 2016: Wind structure discrepancies between two best track datasets for western North Pacific tropical cyclones. *Mon. Wea. Rev.*, **144**, 4533–4551, https://doi.org/10.1175/MWR-D-16-0163.1.

Sriver, R. L., and M. Huber, 2007: Observational evidence for an ocean heat pump induced by tropical cyclones. *Nature*, **447**, 577–580, https://doi.org/10.1038/nature05785.

Vincent, E. M., M. Lengaigne, G. Madec, J. Vialard, S. Masson, N. C. Jourdain, C. E. Menkes, and S. Jullien, 2012: Processes setting the characteristics of sea surface cooling induced by tropical cyclones. *J. Geophys. Res.*, **117**, C02020, https://doi.org/10.1029/2011JC007396.

Wallace, J. M., T. P. Mitchell, and C. Deser, 1989: The influence of sea surface temperature on surface wind in the eastern equatorial Pacific: Seasonal and interannual variability. *J. Climate*, **2**, 1492–1499, https://doi.org/10.1175/1520-0442(1989)002<1492:TIOSST>2.0.CO;2.

Wang, G., L. Wu, N. C. Johnson, and Z. Ling, 2016: Observed three-dimensional structure of ocean cooling induced by Pacific tropical cyclones. *Geophys. Res. Lett.*, **43**, 7632–7638, https://doi.org/10.1002/2016GL069605.

Webster, P. J., G. J. Holland, J. A. Curry, and H.-R. Chang, 2005: Changes in tropical cyclone number, duration, and intensity in a warming environment. *Science*, **309**, 1844–1846, https://doi.org/10.1126/science.1116448.

Wentz, F. J., C. Gentemann, D. Smith, and D. Chelton, 2000: Satellite measurements of sea surface temperature through clouds. *Science*, **288**, 847–850, https://doi.org/10.1126/science.288.5467.847.

Willoughby, H. E., and M. E. Rahn, 2004: Parametric representation of the primary hurricane vortex. Part I: Observations and evaluation of the Holland (1980) model. *Mon. Wea. Rev.*, **132**, 3033–3048, https://doi.org/10.1175/MWR2831.1.

——, R. W. R. Darling, and M. E. Rahn, 2006: Parametric representation of the primary hurricane vortex. Part II: A new family of sectionally continuous profiles. *Mon. Wea. Rev.*, **134**, 1102–1120, https://doi.org/10.1175/MWR3106.1.

Xie, S.-P., M. Ishiwatari, H. Hashizume, and K. Takeuchi, 1998: Coupled ocean-atmospheric waves on the equatorial front. *Geophys. Res. Lett.*, **25**, 3863–3866, https://doi.org/10.1029/1998GL900014.

Xu, J., and Y. Wang, 2015: A statistical analysis on the dependence of tropical cyclone intensification rate on the storm intensity and size in the North Atlantic. *Wea. Forecasting*, **30**, 692–701, https://doi.org/10.1175/WAF-D-14-00141.1.

——, and ——, 2018: Dependence of tropical cyclone intensification rate on sea surface temperature, storm intensity, and size in the western North Pacific. *Wea. Forecasting*, **33**, 523–537, https://doi.org/10.1175/WAF-D-17-0095.1.

Yan, D., and T. Zhang, 2022: Research progress on tropical cyclone parametric wind field models and their application. *Reg. Stud. Mar. Sci.*, **51**, 102207, https://doi.org/10.1016/j.rsma.2022.102207.

Yan, Y., L. Li, and C. Wang, 2017: The effects of oceanic barrier layer on the upper ocean response to tropical cyclones. *J. Geophys. Res. Oceans*, **122**, 4829–4844, https://doi.org/10.1002/2017JC012694.

Zhang, H., D. Chen, L. Zhou, X. Liu, T. Ding, and B. Zhou, 2016: Upper ocean response to Typhoon Kalmaegi (2014).

J. Geophys. Res. Oceans, **121**, 6520–6535, https://doi.org/10.1002/2016JC012064.

——, and Coauthors, 2018: Net modulation of upper ocean thermal structure by Typhoon Kalmaegi (2014). *J. Geophys. Res. Oceans*, **123**, 7154–7171, https://doi.org/10.1029/2018JC014119.

——, and Coauthors, 2020: Sea surface current response patterns to tropical cyclones. *J. Mar. Syst.*, **208**, 103345, https://doi.org/10.1016/j.jmarsys.2020.103345.

Zhang, J., Y. Lin, D. R. Chavas, and W. Mei, 2019: Tropical cyclone cold wake size and its applications to power dissipation and ocean heat uptake estimates. *Geophys. Res. Lett.*, **46**, 10 177–10 185, https://doi.org/10.1029/2019GL083783.

Zhang, X. Y., F. H. Xu, J. S. Zhang, and Y. L. Lin, 2022: Decrease of annually accumulated tropical cyclone-induced sea surface cooling and diapycnal mixing in recent decades. *Geophys. Res. Lett.*, **49**, e2022GL099290, https://doi.org/10.1029/2022GL099290.